Ore Geology Reviews 120 (2020) 103405

Contents lists available at ScienceDirect

Ore Geology Reviews

journal homepage: www.elsevier.com/locate/oregeorev

In-situ sulfur isotope and trace element compositions of pyrite from the Neoproterozoic Haweit gold deposit, NE Sudan: Implications for the origin and source of the sulfur

Munir M.A. Adam[a,*], Xinbiao Lv[a,b,*], A.A. Abdel Rahman[c], Robert J. Stern[d], Asma A.A. Abdalrhman[e], Zaheen Ullah[a]

[a] Faculty of Earth Resources, China University of Geosciences, Wuhan 430074, China
[b] Geological Survey, China University of Geosciences, Wuhan 430074, China
[c] College of Petroleum Geology and Minerals, University of Bahri, Khartoum North 11116 Sudan
[d] Geosciences Dept., U Texas at Dallas, Richardson, TX, USA
[e] ALNA W ATE FOR GOLD&COPPER CO.LTD, Khartoum, Sudan

ARTICLE INFO

Keywords:
Pyrite
LA-ICP–MS
Gold deposit
Origin
Hamisana Shear Zone
NE Sudan

ABSTRACT

The Haweit gold deposit is located in the Neoproterozoic Hamisana Shear Zone in the Red Sea Hills of NE Sudan. In this study, we use major and trace element chemistry of pyrite, SEM studies, as well as the sulfur isotope composition of pyrite from the deposit to characterize the mineralization, origin of the ore-forming fluids and to constrain the ore-forming processes. Mineralization was controlled by NE- and NW-trending faults, which host many gold-bearing quartz veins in the Neoproterozoic andesitic and granitic country rocks. Fluids and melts associated with the quartz veins produced extensive zones of wall-rock alteration a few centimeters to several meters in thickness. The associated hydrothermal alteration is characterized by sericitization, carbonatization, silicification and pyritization. The Au mineralization is closely associated with the alteration zones, in which two generations of hydrothermal pyrite were identified on the basis of morphology; Py1 consisting of anhedral, elongate or spongy grains and Py2 consisting of medium- to coarse-grained, anhedral to subhedral crystals. Py1 is characterized by slighty lower concentrations of Au, whereas Py2 has slightly higher amounts of Au, As, and Zn. Arsenic, Co, Ni and Cu vary in concentration between the two types of pyrite as shown by their Co/Ni ratios ranging from 0.02 to 57 (average 13.5 ppm) in Py1 and from 0.04 to 165 (average 23.4 ppm) in Py2, indicating growth from magmatic-hydrothermal fluids. The $\delta^{34}S$ values of the two types of pyrite are similar, ranging from −3.3 to 3.4‰, with an average value of −0.7‰, suggesting a common, magmatic source for the sulfur. All available data point to a hydrothermal-magmatic source for the Haweit gold deposit.

1. Introduction

Gold mining in the Red Sea Hills of Sudan goes back at least to the time of the Middle Kingdom Egyptian dynasties (Elsamani et al., 2001). The ancient workings for precious stones and gold were mostly developed between 2000 and 1600 BCE (Barbour, 1961; Elsamani et al., 2001). Wadi Allaqi along the Egypt-Sudan border was the principal mining center in Nubia and was worked until the middle of the 12th century (Reclus, 1876). Recently intensive prospecting and exploration by the Geological Research Authority of Sudan (GRAS) have assessed the precious metal potential of the region, and discovered new deposits. In addition, such work provides new information regarding the relationship of gold mineralization with the Neoproterozoic tectonic evolution of the region. Most of the ancient and recent gold mines are located in the northeastern, central and northern parts of the Red Sea Hills region and their distribution is controlled largely by shear zones and major faults. The Neoproterozoic Arabian–Nubian Shield (ANS) in northeast Africa and Arabia consists predominately of juvenile continental crust of Neoproterozoic age (Fig. 1A) (Dixon & Golombek, 1988; Stern et al., 1990; Hargrove et al., 2006; Al-Hwaiti et al., 2010). This region formed essentially by accretion of volcanic island arcs in Late Tonian through Cryogenian time, with further magmatic additions in Ediacaran time. Igneous activity was accompanied by extensive hydrothermal activity (Almond et al., 1984; Tolessa & Pohl, 1999; Kusky

* Corresponding authors at: Faculty of Earth Resources, China University of Geosciences, Wuhan 430074, China.
E-mail addresses: munirkonil@hotmail.com (M.M.A. Adam), luxb@cug.edu.cn (X. Lv), abdahabd@yahoo.com (A.A. Abdel Rahman), rjstern@utdallas.edu (R.J. Stern), asmaabdalrhman90@hotmail.com (A.A.A. Abdalrhman), zaheengeo@gmail.com (Z. Ullah).

https://doi.org/10.1016/j.oregeorev.2020.103405
Received 1 December 2019; Received in revised form 2 February 2020; Accepted 10 February 2020
Available online 14 February 2020
0169-1368/

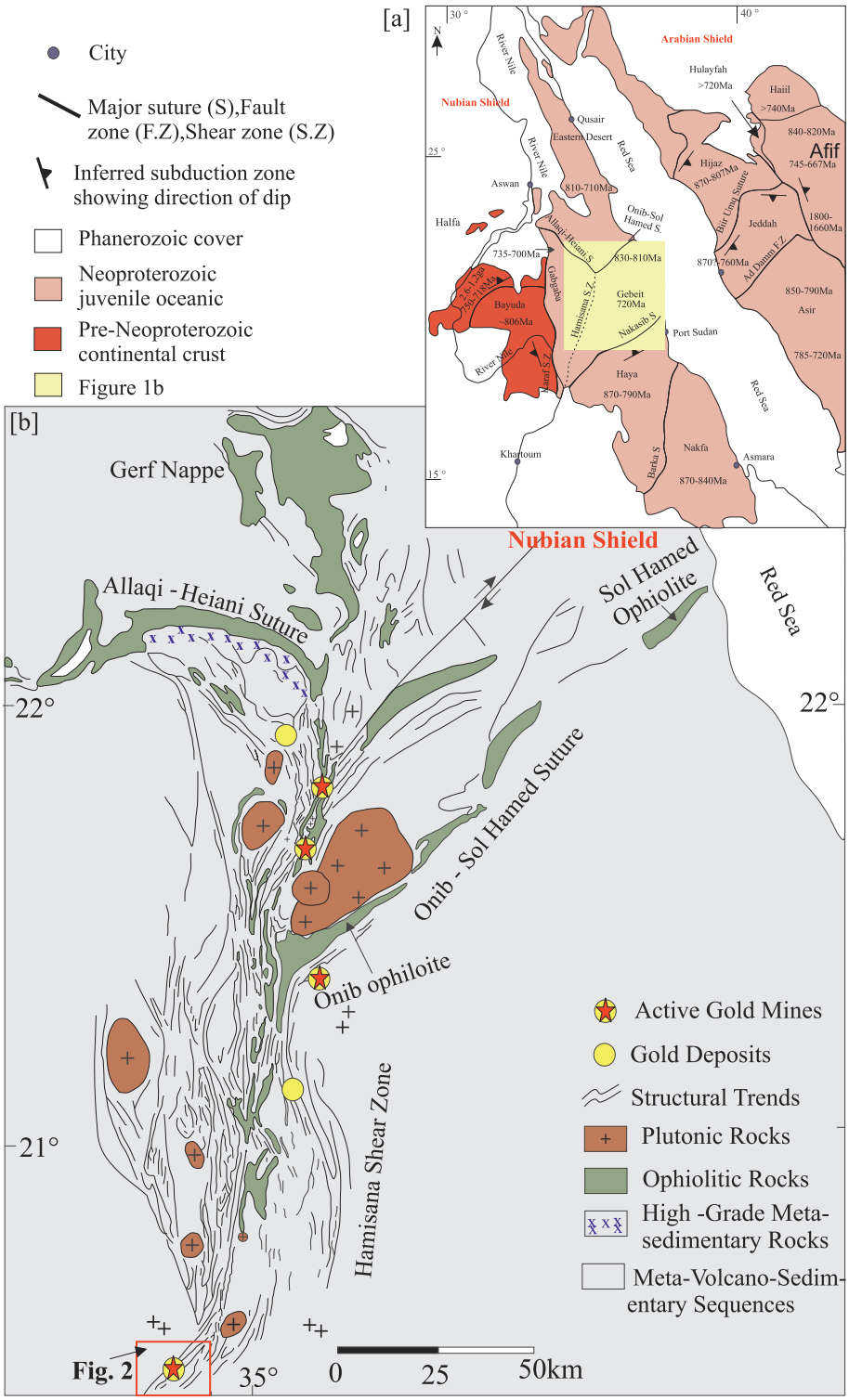

Fig. 1. Regional geologic setting. A) Arabian-Nubian Shield showing distribution of juvenile Neoproterozoic continental crust and older crust that was thermally reprocessed in Neoproterozoic time. Location of B) shown by yellow box. B) Geological map of the Hamisana shear zone, the eastern part of the Allaqi-Heiani suture, and the locations of other working gold mines in the Hamisana Shear Zone (modified after Stern et al., 1990). Location of Fig. 2 is also shown.

& Ramadan 2002; Sami et al., 2017).

An overview of ANS gold mineralization can be found in Johnson et al. (2017). The ~150 km long N-S trending Hamisana Shear Zone (Fig. 1) stands out among the auriferous shear zones in the region. Johnson et al. (2017) classified gold mineralization in the Hamisana shear zone as orogenic gold deposits. Orogenic gold is typically associated with low-grade, sheared volcanic, volcaniclastic, and epiclastic rocks. The Haweit gold deposit (Fig. 1) is one of several orogenic gold deposits found along the Hamisana Shear Zone; little is known about these deposits. We focus on pyrite in the Haweit deposit to better understand Hamisana orogenic gold mineralization.

Pyrite is one of the dominant sulfide mineral in the Earth's crust and it is found in a wide variety of geological settings (Craig & Vokes, 1993). Importantly, it is also one of the main constituents of

hydrothermal mineralization in many gold deposits, including orogenic, epithermal, mesothermal and Carlin-type (Reich et al., 2013). In sedimentary rocks pyrite forms nano- to micro-size framboids that may grow into well-developed, euhedral cubic crystals during diagenesis and low-grade metamorphism. Pyrite also plays an important role in hydrothermal systems by causing enrichment in supergene Cu-Au deposits. Pyrite is the most common sulfide ore mineral in orogenic gold deposits, it is also widespread in various quartz veins, alteration zones and associated host rocks. This mineral also contains a wide variety of trace elements (i.e., Ag, As, Au, Bi, Co, Cu, Pb, Zn, Ni, Sb, and Te) that occur in different forms, such as solid solution, nanoparticles, nano-inclusions and clusters (Large et al., 2009; Thomas et al., 2011; Reich et al., 2013; Deditius et al., 2014; Gregory et al., 2014; Zhu et al., 2017).

Due to its refractory nature, pyrite can preserve changing fluid compositions during different stages of its growth. Consequently, pyrites commonly exhibit compositional zoning and variations in the abundance and variety of mineral inclusions. Such zoning may be revealed by variations in reflectivity and trace element compositions in mineral inclusions (Craig et al., 1998; Belcher et al., 2004; Large et al., 2007).

Trace elements in sulfide minerals are particularly useful for documenting changes in physicochemical conditions of hydrothermal fluids, which in turn, may provide clues to geodynamic settings and genetic relationships between mineralization and the host rocks (Maslennikov et al., 2009; Hannington, 2014; Keith et al., 2016; Monecke et al., 2016).

In addition to As, Co, Cu and Ni, many other trace elements may be unequally distributed in pyrite revealing enriched and depleted zones. Compositional mapping of such zones can provide crucial information on the history of pyrite growth and the relative time of transport of specific elements in the ore fluids (Craig et al., 1998; Cook et al., 2009; Sung et al., 2009; Thomas et al., 2011; Reich et al., 2013).

Gold and arsenic are strongly coupled in pyrite from many different types of ore deposits, especially orogenic (Large et al., 2007; Morey et al., 2008), epithermal (Cook & Chryssoulis, 1990; Deditius et al., 2008; Reich et al., 2013), and Carlin type (Cline, 2001; Emsbo et al., 2003; Reich et al., 2005; Muntean et al., 2011), as well as in volcanogenic massive sulfides (VHMS) (McClenaghan et al., 2004). The maximum amount of gold that can be hosted in pyrite is mostly a function of the arsenic concentration (Reich et al., 2005), but other factors, such as grain size, alteration, temperature of formation, and the abundance of other trace elements can also play a role (Mumin, et al., 1994; Fleet & Mumin, 1997; McClenaghan et al., 2004; Reich et al., 2005; Reich & Becker, 2006; Large et al., 2007; Deditius et al., 2008; Maslennikov et al., 2009; Deditius et al., 2011).

This study presents the first research on the Au and other trace element concentrations in pyrite from the Haweit gold deposit. We report the mineralogy and mineral assemblages of the ore deposit, as well as trace element and sulfur isotopic compositions. We use EPMA, LA-ICP-MS, SEM, and in-situ sulfur isotopes to determine the systematic differences, range and distribution of trace elements content between different generations of pyrite in order to constrain the origin of the ore-forming fluids, and ultimately to trace evolution of the ore-forming processes.

2. Geological setting

2.1. Regional geology

The study area lies in the Red Sea Hills, which is part of the Arabian Nubian Shield (ANS) of NE Africa. The ANS is recognized as one of the large orogenic belts that formed during the Neoproterozoic assembly of Greater Gondwana (Stern, 1994), and it covers a very wide area extending, with the Red Sea closed, from the River Nile actoss the Red Sea Hills of Sudan and the Eastern Desert of Egypt to the eastern edge of the Arabian Shield. It also includes large areas in the western and central parts of Saudi Arabia, Eritrea, Yemen, and parts of northern Ethiopia (Kröner et al., 1987; Vail, 1988). It is generally agreed that the ANS was formed by the accretion of several intra-oceanic microplates, due to subduction-related processes and collision tectonics during the Neoproterozoic to early Paleozoic Pan-African orogeny between 900 and 500 Ma (Stoeser & Camp, 1985; Vail, 1988; Rahman, 1993). Generally, the ANS is characterized by extensive calc-alkaline, volcanogenic sequences of island arc geochemistry and related sediments that formed distinct terranes. The terranes later collided along linear sutures marked by mafic-ultramafic rocks of dismembered ophiolite complexes and intruded by syn- to late-orogenic, calc-alkaline granitoids and post-orogenic complexes (Fig. 1).

The ANS was subjected during the various stages of its evolution to polyphase folding, thrusting and shearing. The consolidated juvenile terranes of the ANS were accreted to the west against the pre-Neoproterozoic continental margin of the so- called “Nile Craton” (Rocci, 1965), the East Saharan Craton (Schandelmeier et al., 1988), the African Craton (Rahman, 1993) or the Saharan metacraton (Abdelsalam et al., 2002). This older domain is a different geodynamic environment that represents a sialic continental plate with high-grade gneissic rocks (Vail, 1988) and evolved isotopic compositions. The Hamisana Shear Zone is thought to have formed as a result of shortening related to this collision sometime between 670 and 610 Ma (Stern and Kröner, 1993). Hamisana Shear Zone gold mineralization happened before, during and after this deformation; Haweit mineralization occurred during or after deformation.

2.2. Mining district geology

The Haweit deposit lies in the southernmost Hamisana Shear Zone (Fig. 1). Previous studies of mineralization in this region are mostly limited to the geological and geotectonic classification of the gold deposits (Elsamani et al., 2001), and the petrogenesis of the magmatic rocks hosting the Cu-Au mineralization (Bierlein et al., 2016). The study area is dominated by Neoproterozoic low-grade metamorphic volcano-sedimentary sequences and, gabbroic to granodioritic plutonic rocks overlain by Quaternary deposits (Figs. 2 and 3). The Haweit deposit is hosted in sericite-chlorite schists and Neoproterozoic andesitic and granitic rocks. Andesitic rocks are widely distributed as layers or large lenses. They are grayish, porphyritic rocks with a blocky structure, composed chiefly of feldspar, pyroxene, olivine and hornblende, with lesser amounts of biotite, magnetite, and pyrite (Fig. 4a, c and d). Small amounts of sericite, calcite, epidote and chlorite are also present. Plagioclase forms subhedral to euhedral phenocrysts that, in some cases, exhibit lamellar twinning. Basaltic andesite only occurs west of mine No.1 (Fig. 2). It is a distinctive, fine-grained rock with abundant phenocrysts of plagioclase, olivine and pyroxene (Fig. 4b). Pyrite and magnetite occur as accessory minerals, and secondary minerals include chlorite, calcite, and sericite.

Granites are mainly in the middle and southern parts of the study area (Fig. 2). They are pale red to pinkish, medium-grained, massive rocks with average modal compositions of K-feldspar (45–55%), plagioclase (10–15%) and quartz (39%), with small amounts of microcline, epidote, sericite, calcite, chlorite, magnetite, and pyrite (Fig. 4e and f); traces of biotite, perthite, muscovite, sphene and zircon are also locally present. Both mafic and felsic veins intrude the metamorphic rocks, where they trend NE and NW. Quaternary sediments, including conglomerate, fluvial gravels and aeolian sand sheets, cover large parts of the area. These are mostly 10 to 60 cm thick but may be up to 2 m in some areas, such as deep channels or wadis.

Based on their trend and shape, we divide Au-bearing quartz veins in the Haweit mine into three generations: (1) NEE-trending, reddish quartz veins (early stage) (Fig. 5a), (2) EW-trending, gray quartz veins (middle stage) (Fig. 5b) and (3) NW- trending, milky-colored quartz veins (last stage) (Fig. 5c). These Au-bearing quartz veins are hosted in schist, andesitic, and granitic rocks. Generally, the ore bodies are

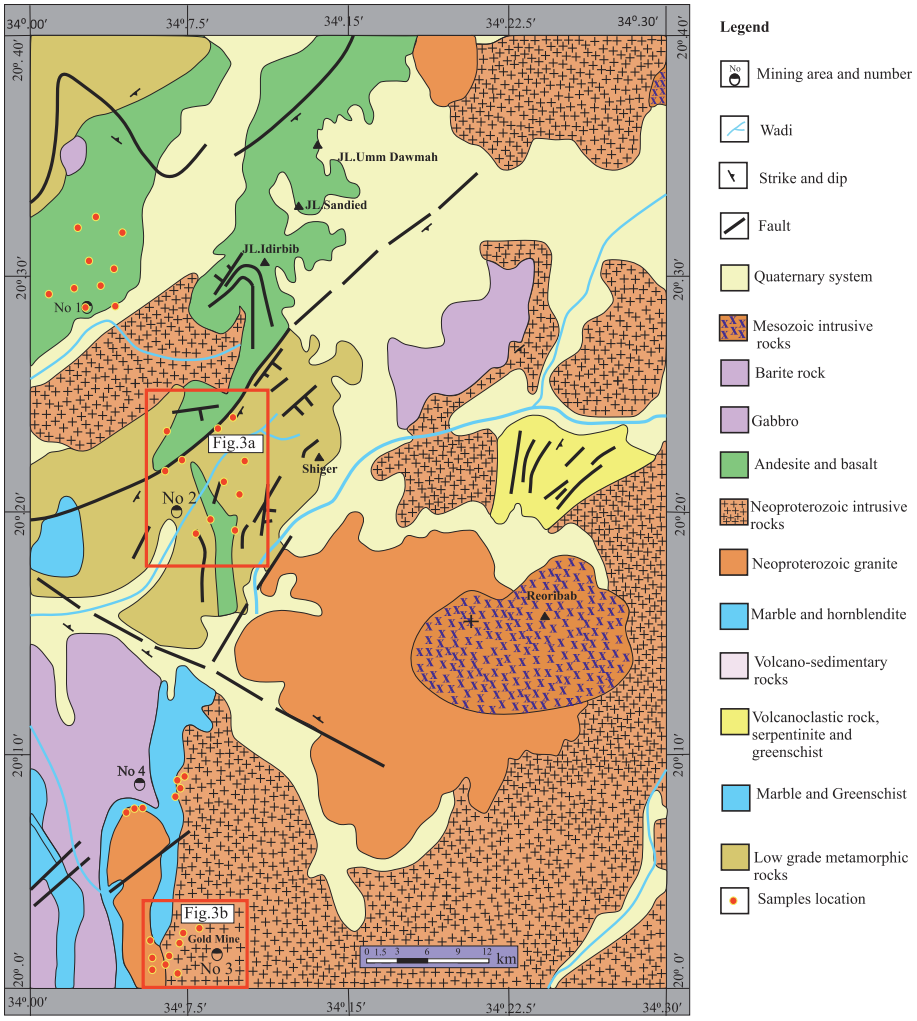

Fig. 2. Geological maps of the Haweit gold deposit (Block 16), showing lithology distribution, regional structures and location of prospective areas (gold mine). Two areas of detail shown in Fig. 3 are also shown. Note that Fig. 3A is mostly in a region of low-grade metamorphic rocks whereas Fig. 3B is mostly in an area of Neoproterozoic intrusive rocks.

controlled by geological structures such as shear zones, faults, and joints, and range in thickness from few centimeters to several meters. They typically consist of quartz, pyrite, chalcopyrite, galena, tetrahedrite, chalcocite, covellite, native gold and silver. Gold mineralization is closely associated with alteration zones. Wall rock alteration is well developed along shear and fault zones, and includes sericitization, carbonatization, silicification, and pyritization. Sericitization is the most common alternation type and is well developed in the area. It mainly occurs in the centers of the altered zones. Pyrite is common in all generations of mineralization and typically occurs as small, disseminated cubes filling fractures 2–15 mm wide. Pyrite is one of the most important ore-bearing minerals containing gold in these deposits.

Carbonatization is mostly found in altered cataclastic zones where it marks the end of gold mineralization. Alteration of hydrous Fe, Mg and Al silicate minerals in these zones released Fe, Mg, Al, Na, and Ca, which combined with CO_2 in the solutions to form calcite, ankerite and siderite. This process also released silica, which was then deposited as quartz veins Fig. 6.

Petrographically, Haweit ores consist of gangue and metallic minerals, and the mineralogy of the ores varies from one generation to another (Fig. 7). Gangue minerals are more than 95% of the ore and consist chiefly of quartz, K-feldspar, plagioclase, sericite, chlorite, calcite, pyroxene, olivine, hornblende, biotite, and epidote (Fig. 4). Metallic minerals in the ore rarely exceed 4% and consist of pyrite, chalcopyrite, arsenopyrite, tetrahedrite, magnetite, covellite, chalcocite, native gold, and silver (Fig. 6). Pyrite is the dominant sulfide mineral in the ore bodies, with lesser amounts of arsenopyrite, galena and chalcopyrite. Pyrite occurs in two textural varieties: (1) small, anhedral, elongate to spongy grains (Py1); and (2) medium to coarse, anhedral to subhedral grains (Py2). Py1 ranges from 30 μm to 500 μm in diameter, and occurs as aggregates or isolated grains commonly overgrown by Py2 (Fig. 6a, c, h and i). Py2 ranges in size from 50 μm to 600 μm (Fig. 6a, c, h and i). Chalcopyrite occurs as anhedral to subhedral grains or inclusions, as well as fracture fillings in pyrite aggregates (Fig. 6a, b and c). Galena is one of the most important sulphide minerals in the Haweit mine area. It occurs as irregular grains in contact with pyrite, tetrahedrite and chalcopyrite or as isolated grains. Galena is generally intergrown with pyrite and associated with native gold (Fig. 6a, d, e and g). Arsenopyrite occurs as small (10 to 30 μm), anhedral grains typically intergrown with pyrite, and is associated with native gold (Fig. 6c). Covellite and chalcocite are minor phases in the ore samples. The covellite occurs as anhedral grains and inclusions associated with galena and silver (Fig. 6e, f and g), whereas the chalcocite mainly occurs with overgrowths of coellite (Fig. 6e and g). Native gold is rare but does occur in some quartz veins (early stage samples), where it fills fractures in pyrite (Fig. 6c and d). Tetrahedrite occurs as rare, fine-grained, anhedral to subhedral phases associated with pyrite, galena and chalcopyrite (Fig. 6b and d). Native silver is a minor phase that occurs mostly in quartz veins (last-stage samples) and generally is elongate to rounded in form (Fig. 6f).

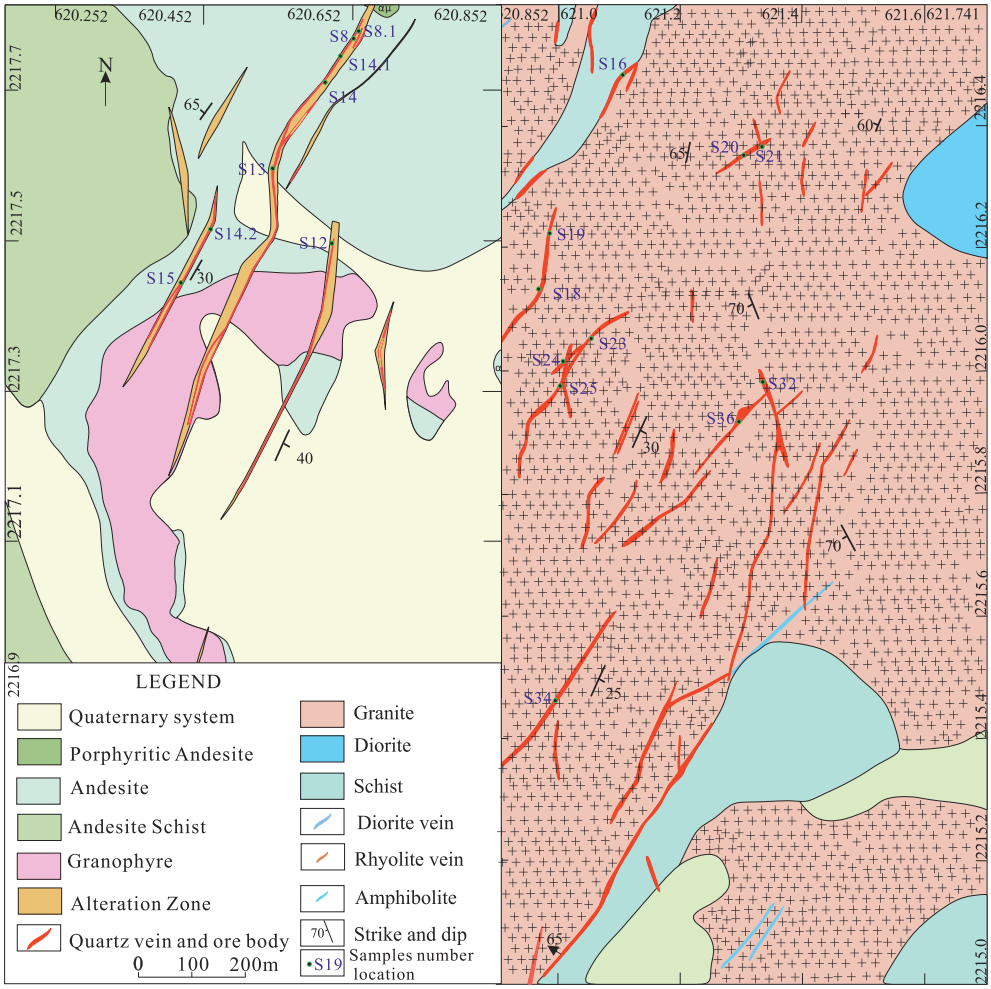

Fig. 3. detailed geological maps of mine area. (a) Geological map of mine area No.2. and (b) Geological map of mining area No.3.

3. Analytical techniques

3.1. Ore microscopy and SEM analyses

The ore mineralogy of Haweit gold deposit was mapped in the field and the textural characteristics examined petrographically using polished rock mounts and polished thin sections of ore samples. Further examination was made using a EVO LS 15 scanning electron microscope (SEM) equipped with the Aztec X-Max 20 energy dispersive spectrometer at the Key Laboratory of Tectonic and Petroleum Resources Ministry of Education at China University of Geosciences (CUG). The operating conditions for BSE were 25 kV acceleration and 100 μA beam current, and the I Probe was 500 pA, the spot size was 480 μm.

3.2. In-situ SIMS sulfur isotope analysis

In-situ sulfur isotope analysis of different stages of pyrite in thin sections was carried out using a LA-MC-ICP-MS at the State Key Laboratory for Geological Processes and Mineral Resources (GPMR) at the China University of Geosciences (Wuhan), using a 193 nm New Wave ArF Excimer laser coupled with a Neptune Plus MC-ICP-MS. Helium gas was used to transport the ablated materials into the plasma with a gas flow of 0.7 L/min. Sample gas (argon, 0.85 L/min) was mixed with the carrier gas in a cyclone coaxial mixer before being transported into the ICP torch. The energy flNe-MS of the laser is approximately 3 J/cm2. Integration time of the isotope was set at1.023 s, and the MC-ICP-MS was operated in the medium-resolution mode to separate polyatomic interferences (e.g., $^{16}O^{2+}$, $^{1}H^{32}S^{+}$, $^{16}O^{17}O^{+}$, $^{1}H^{16}O^{16}O^{+}$, $^{16}O^{18}O^{+}$ etc.) from ^{32}S, ^{33}S to^{34}S. For single spot analysis, the diameter was 23 μm with a laser repletion rate of 8 Hz. The low background of less than 70 mV on ^{32}S was compared to approximately 20 V of signal (for pyrite samples) and the fast “washout” time of 25 s allowed a high sample throughput. The precision of $^{34}S/^{32}S$ analyses is better than 0.00003 (1δ). An in-house pyrite standard (WS-1), consisting of a natural pyrite crystal from the Wenshan polymetallic skarn deposit in Yunnan Province, south China, was used to calibrate the mass bias for S isotopes. The $^{34}SV\text{-}_{CDT}$ values (0.3 ± 0.1‰) for WS-1 natural pyrite were determined using the CF-IRMS method on a MAT 253 isotope ratio mass spectrometer (Thermo Finnigan, Bremen, Germany) at the Institute of Mineral Resources, Chinese Academy of Geological Sciences, Beijing (Zhu et al., 2017). Standards were measured before and after every four spot analyses. The analytical precision is estimated to be better than 0.5‰. The results of the LA-MC-ICPMS analyses are presented in Table A5.

3.3. EMPA analyses

Mineral compositions of pyrite were analyzed by a JEOL JXA-8100 electron microprobe (EPMA) with four wavelength-dispersive spectrometers (WDS) at the State Key Laboratory of Geological Processes and Mineral Resources (GPMR), China University of Geosciences (Wuhan). The microprobe was operated at an accelerating voltage of 20 kV, a beam current of 20 nA, and a beam diameter of 1 μm. The spectral lines and detection limits (ppm) for each element are: Fe (FeS2, Kα, 129), S (FeS2, Kα, 56), As (GaAs, Lα, 224), Co (Co, Kα, 124), Ni (Ni, Kα, 134), Ag (Ag, Lα, 189), and Au (Au, Lα, 247). The following standards were

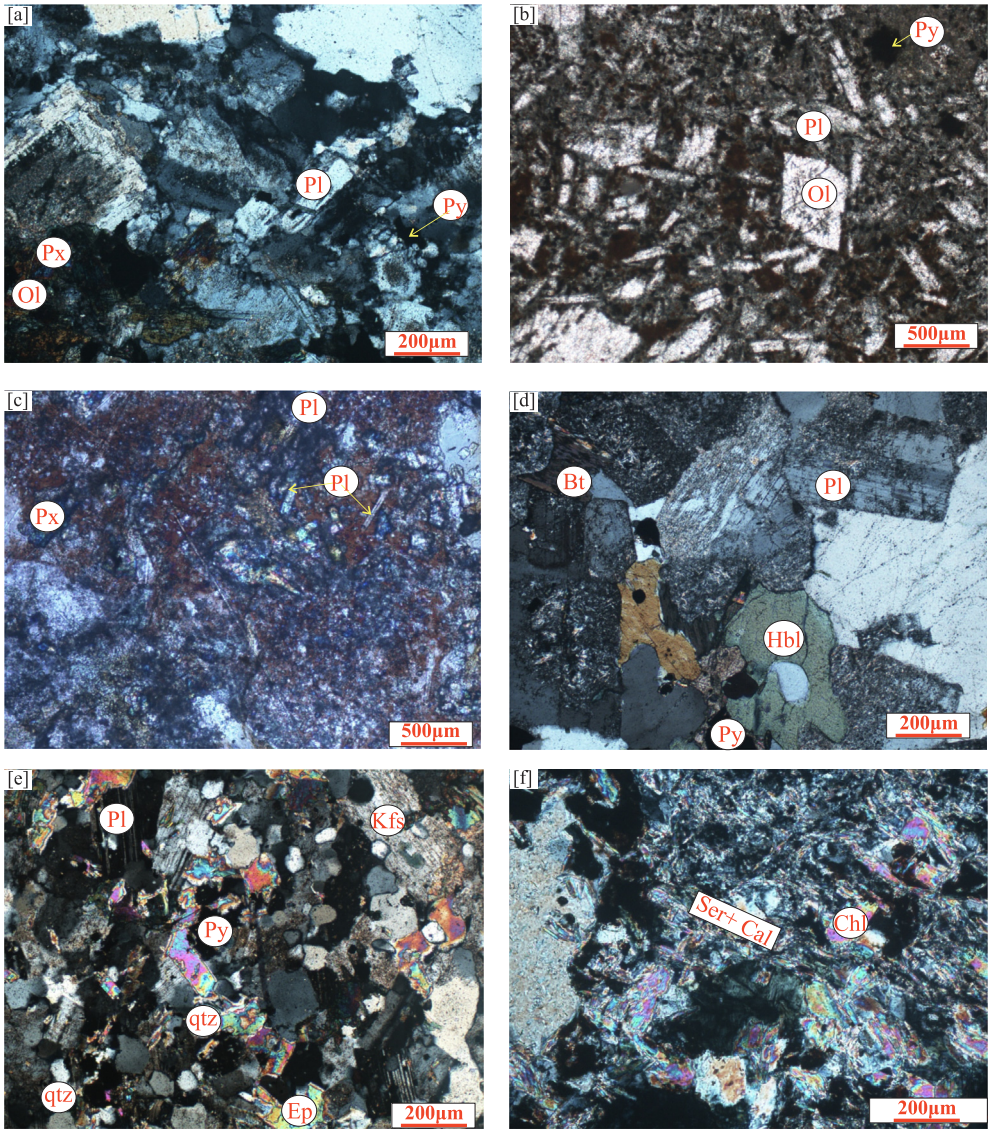

Fig. 4. Photomicrographs of Haweit volcanic rocks: (a) Plagioclase phenocrysts with pyroxene, olivine and pyrite in andesite. (b) Olivine embedded between plagioclase crystals in basaltic andesite. (c) Plagioclase laths with pyroxene in andesite (d) Hornblende, biotite and pyrite with plagioclase phenocrysts (albite). (e) K-felspar, quartz, plagioclase, and pyrite under crossed nicols in granite. (f) Shows chlorite and sericite -calcite vein in granite rock. Pl = Plagioclase, Qtz = quartz, Kfs = k-feldspar, Py = pyrite, Chl = chlorite, Ser = sericite, Cal = calcite, Px = Pyroxene, Ol = Olivine, Hbl = Hornblende, Bt = Biotite.

used for the calibration of elemental X-ray intensities: gallium arsenide (As), pyrite (S,Fe), copper (Cu), antimony (Sb), cobalt (Co), nickel (Ni), bismuth (Bi), molybdenite (Mo), gold (Au), galena (Pb), and silver (Ag). The resulting data were corrected on-line using a ZAF (atomic number, absorption, fluorescence) correction procedure.

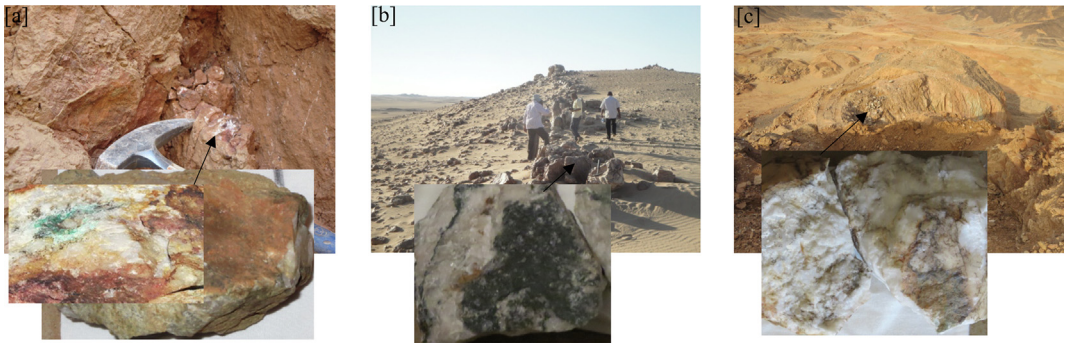

Fig. 5. Representative photographs of the mineralization types. (a) NEE- trending reddish quartz vein (early stage) (b) EW- trending gray quartz vein (middle stage), and (c) NW- trending milky quartz vein (last stage).

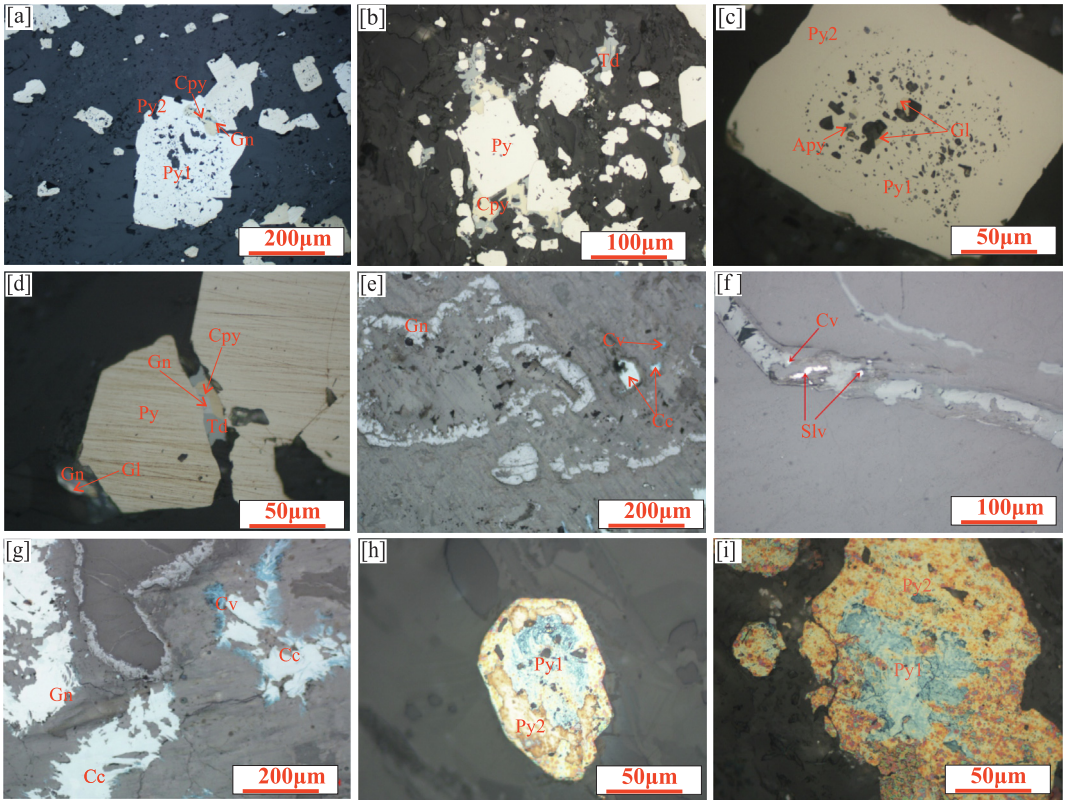

Fig. 6. Reflected light photomicrographs showing mineral assemblages and textures of pyrite types in the Haweit gold deposit. (a) Coexistence of chalcopyrite and galena with pyrite. (b) Coexistence of tetrahedrite with pyrite and coexistence of chalcopyrite with pyrite. (c) Disseminated inclusions of native gold and arsenopyrite a grain of Py1 mantled by Py2. (d) Anhedral to subhedral grains of Py2 with inclusions of chalcopyrite, tetrahedrite, galena and pyrite, coexisting with native gold and galena. (e) Silver vein with chalcocite and covellite. (f) Silver ore with covellite. (g) Galena, chalcocite and covellite. (h) and (i) are photomicrographs of NaOCl-etched pyrite illustrating variations in habit. Red to orange color corresponds of low-Au pyrite; light blue to white colors correspond to high-Au arsenian pyrite. Gl = Native gold. Cv = covellite. Py = pyrite. Ccp = Chalcopyrite. Apy = Arsenopyrite. Gn = Galena. Td = tetrahedrite. Cc = chalcocite. Slv = silver. Py1 = pyrite type 1, Py2 = pyrite type 2.

3.4. In-situ LA-ICP-MS trace element analysis

Trace element analyses of sulfides were conducted with a LA-ICP-MS at the Wuhan Sample Solution Analytical Technology Co., Ltd., Wuhan, China. Detailed operating conditions for the laser ablation system and the ICP-MS instrument and data reduction are the same as those described by (Zong et al., 2017). Laser sampling was performed using a GeolasPro laser ablation system that consists of a COMPexPro 102 ArF excimer laser (wavelength of 193 nm and maximum energy of 200 mJ) and a MicroLas optical system. An Agilent 7700e ICP-MS

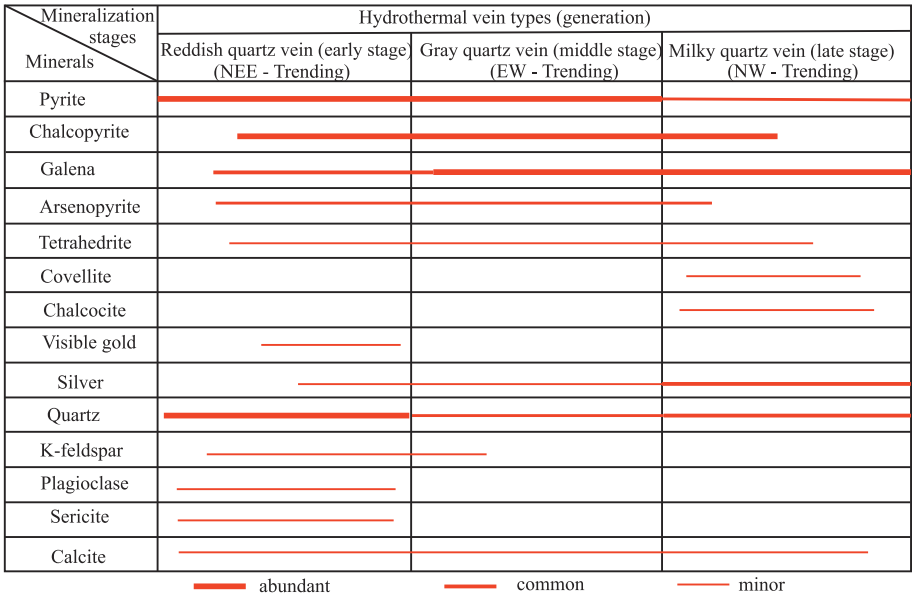

Fig. 7. The paragenetic sequence of gangue and ore minerals for the Haweit gold deposit.

instrument was used to acquire ion-signal intensities. Helium was applied as a carrier gas. Argon was used as the make-up gas and mixed with the carrier gas via a T-connector before entering the ICP. A "wire" signal smoothing device is included in this laser ablation system (Hu et al., 2014). The spot size and frequency of the laser were set to **32** μm and **5/6** Hz, respectively. Trace element compositions of sulfides were calibrated against various reference materials (NIST 610 and NIST 612) without using an internal standard (Liu et al., 2008). The sulfide reference material of MASS-1 (USGS) was used as the unknown sample to verify the accuracy of the calibration method. Each analysis incorporated a background acquisition of approximately 20–30 s followed by 50 s of data acquisition from the sample. An Excel-based software ICPMSDataCal was used to perform off-line selection and integration of background and sample signals, time-drift correction and quantitative calibration for trace element analysis (Liu et al., 2008).

4. Results

4.1. In situ sulfur isotopic compositions of pyrites

A total of 24 sulfur isotopic compositions of pyrites were measured, including 12 Py I, and 12 Py 2. The results are listed in Table 1 and shown in Fig. 8. Py1 has $\delta^{34}S$ values of −3.3‰ to +3.4‰, with a median $\delta^{34}S$ −0.15‰ and show a distinct normal distribution, whereas Py2 is characterized by slightly lower $\delta^{34}S$ values from −3.2‰ to 0.6‰, with a median of $\delta^{34}S$ −1.4‰, although still within the same isotopic range as Py I (Fig. 8). The sulfur isotopic compositions in individual pyrite grains are homogeneous.

4.2. Electron microprobe analyses of pyrite

Electron microprobe data were obtained for the two generations of pyrite (Table 2). The mean values of As, S, Fe and Mo are 0.07 wt%, 52.09 wt%, 46.02 wt%, and 0.71 wt%, respectively for Py1 and 0.06 wt %, 52.33 wt%, 46.11 wt%, and 0.68, respectively, for Py2. The S/As ratio is ~1250 for Py1 and ~1500 for Py2. Concentrations of Au and other trace elements (Co, Ni, Cu, Pb, Bi, Sb, and Ag) in pyrite are close to or below the detection limits. No obvious correlation between S and As was observed (Fig. 12f). The EPMA data for pyrite (As, Ni, Co) can be used to interpret its crystallization history (Peng & Frei, 2004). Py1 shows a negative correlation between sulfur and arsenic, but gold and cobalt show no clear pattern of distribution (Fig. 9). In Py2 arsenic shows no clear correlations with other elements, but cobalt and gold display primary crystallographic growth bands (Fig. 10).

Table 1
LA-MC-ICP-MS sulfur isotopic compositions of pyrites from the Haweit gold deposit.

Sample	Spot No.	Pyrite stage	$\delta^{34}S$ (‰)
S19	1	Py1	2.8
	2	py2	0.6
S32	1	Py1	−0.1
	2	py2	−0.7
S13	1	Py1	−1.5
	2	py2	−1.4
S16	1	Py1	0.2
	2	py2	−3.2
S18	1	Py1	−1.4
	2	py2	−1.2
S15	1	Py1	1.6
	2	py2	−1.5
S12	1	Py1	−0.2
	2	py2	−0.1
S14-2	1	Py1	3.4
	2	py2	1.4
	4	Py1	−3.3
	5	py2	−1.9
	6	Py1	−2.9
	7	py2	−1.6
S8	1	Py1	0.04
	2	py2	−0.4
S36	1	Py1	−2.5
	2	py2	−2.9

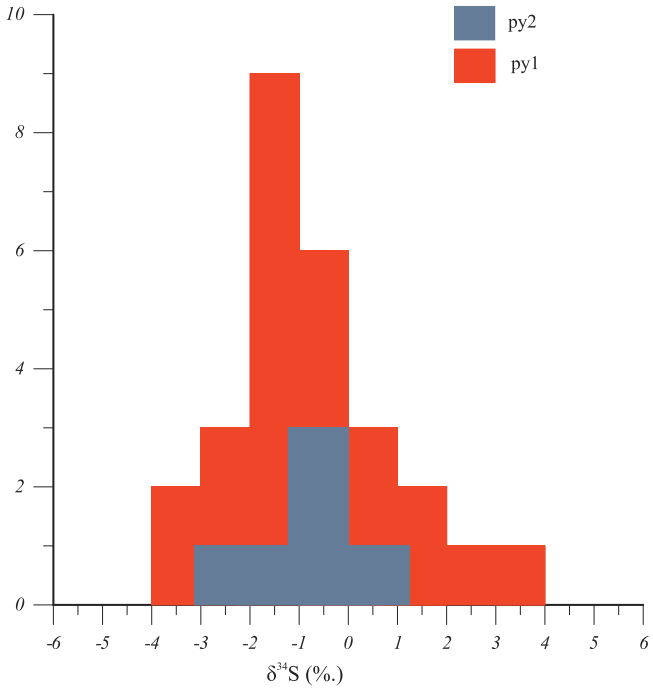

Fig. 8. Histogram of in-situ sulfur isotope data of pyrite from Haweit gold deposit.

4.3. In-situ LA-ICP-MS trace element data

The LA-ICP-MS trace element compositions of the two types of pyrite are summarized in Table 3 and variations of representative elements are illustrated in Fig. 11. Py1 has low contents of Au (0.002–8.2 ppm with a mean of 0.7 ppm), and Mo (0.004–19 ppm) but higher contents of Co (0.005–1059 ppm), Ni (0.05–284 ppm), Sb (0.0–149 ppm), Ag (0.0003–166 ppm), Se (1.63–217 ppm) and significantly higher contents of As (0.27–26,500 ppm), Cu (0.05–9595 ppm), Zn (0.31–9553 ppm) and Bi (0.002–445 ppm).

Py2 contains slightly higher abundances of Au (0.003–10.8 ppm, mean 1.1 ppm), Zn (0.4–11,000 ppm), and As (0.8–28,700 ppm) but lower contents of Cu (0.3–417 ppm), Co (0.03–69 ppm), Ni (0.4–72 ppm), Ag (0.01–58 ppm), Pb (4.4–925 ppm), Sb (0.01–107 ppm), Se (1.3–96 ppm) and Bi (0.18–129 ppm).

Variation diagrams between Au and As, Ag, Cu, Sb and Bi (Fig. 12) show that Py1 contains on average lower contents of Au, Cu, Sb and Bi, whereas Py2 has higher contents of Au, Cu, Sb and Bi. Py2 also shows strong positive correlations between Au and As, Cu and Bi (Fig. 12a, 12c and 12e respectively).

5. Discussion

5.1. Trace element characteristics of pyrite

Pyrite is a common sulfide phase associated with most hydrothermal systems, and its precipitation can control the distribution of a wide array of elements of both economic and environmental importance, such as Ag, As, Au and other metals (Large et al., 2009; Deditius et al., 2011; Ward et al., 2017; Voute et al., 2019). Previous studies show that trace elements in pyrite can occur in many different

Table 2
Selected EPMA analyses of two generations of pyrite from the Haweit gold deposit (wt %).

Pyrite type		As	S	Fe	Bi	Co	Sb	Ni	Pb	Cu	Au	Mo	Ag
Py1	Min.	0.02	51.66	45.16	0.01	0.07	0.02	0.01	0.01	0.01	0.01	0.62	0.01
	Max.	0.21	52.79	46.46	0.14	0.23	0.06	0.07	0.06	0.57	0.12	0.71	0.04
n = 12	Mean	0.07	52.09	46.02	0.06	0.11	0.04	0.03	0.03	0.06	0.04	0.68	0.02
	SD	0.06	0.31	0.38	0.04	0.05	0.01	0.02	0.02	0.16	0.03	0.02	0.01
Py2	Min.	0.02	51.92	45.49	0.01	0.07	0.01	0.01	0.01	0.00	0.01	0.62	0.01
	Max.	0.21	52.74	46.55	0.10	0.26	0.02	0.02	0.07	0.05	0.10	0.72	0.04
n = 9	Mean	0.06	52.33	46.11	0.04	0.13	0.01	0.01	0.01	0.02	0.04	0.68	0.01
	SD	0.05	0.29	0.30	0.03	0.07	0.01	0.01	0.01	0.01	0.03	0.03	0.01

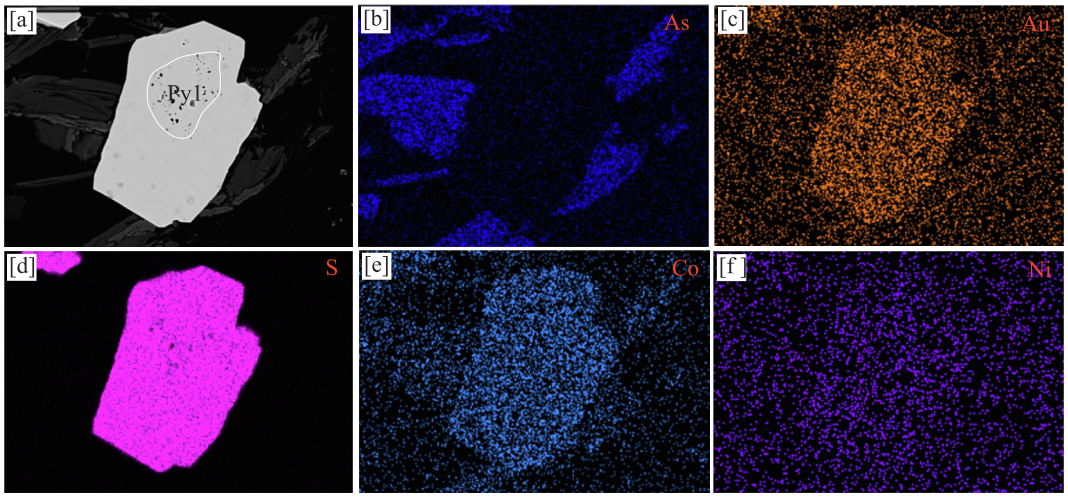

Fig. 9. (a) Backscattered electron image of Py1 surrounded by Py2 from sample S36. (b–f) show X-ray element distribution maps of Co, Ni, S, As, and Au in Py1. Cobalt and nickel have a uniform distribution, but irregular arsenic enrichment occurs in isolated crystal Py1.

ways: (1) micro- to nano-size mineral inclusions (Thomas et al., 2011; Sykora et al., 2018); (2) structurally bound elements (solid solution within the crystal lattice) (Reich et al., 2013; Deditius et al., 2014); and (3) within nanoparticles of sulfides (Ciobanu et al., 2012; Mikhlin & Romanchenko, 2007). Thus, accurate determination of where different trace elements are sequestered in pyrite is important for investigating the influence of mineral inclusions on pyrite chemistry, metal distribution and mineralization processes. In this study, the non-uniform enrichment of trace elements reflects the variability of different metals in different types of pyrite (Py1, Py2). Py1 occurs as small, disseminated grains with irregular or elongate shapes enclosed in oscillatory zoned Py2. Oscillatory zoning in pyrite has been observed in many gold deposits around the world, where it has been interpreted as being due to crystallographic incorporation of trace elements controlled by growth rate (Barker & Cox, 2011; Fougerouse et al., 2016) or to chemical evolution of the hydrothermal fluid (Barker et al., 2009; Peterson & Mavrogenes, 2014). As presented earlier and shown in Fig. 11, concentrations of Au, Ag, As, Pb, Cu, and Bi vary widely but are not systematically different between Py1 and Py2. Sulfur isotopic compositions are also indistinguishable between Py1 and Py2. This suggests that fluid sources, processes and compositions that formed Py1 and Py2 were broadly similar. Trace element profiles for Py1 show

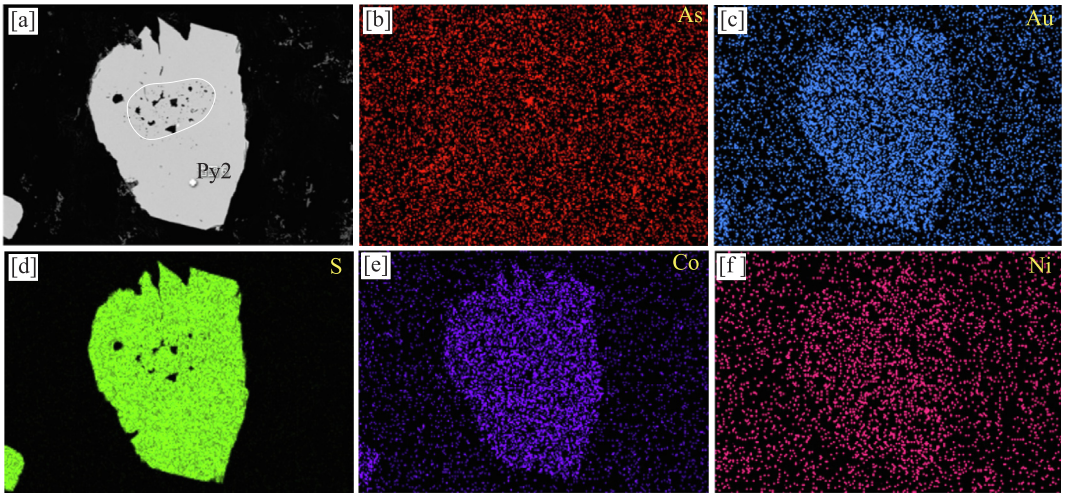

Fig. 10. (a) Backscattered electron image of Py2 (b–f) X-ray element distribution maps of Co, Ni, S, As, and Au in Py2. Cobalt and nickel show uniform distribution, but irregular arsenic enrichment occurs in isolated crystal Py2.

Table 3
Selected LA-ICP-MS analyses of two generations of pyrite from the Haweit gold deposit (ppm).

Pyrite type		Fe	Co	Ni	Cu	Zn	As	Se	Mo	Ag	Sb	Au	Bi	Pb	Co/Ni
Py1	Min.	601.7	0.005	0.05	0.05	0.31	0.27	1.63	0.004	0.003	0.01	0.002	0.002	0.04	0.02
	Max.	628099.5	1058.8	284.3	9594.9	9552.6	26499.4	217.2	19.3	106.6	148.6	8.2	444.6	8245.2	56.8
n = 30	Mean	513029.8	254.8	48.9	734.5	415.9	1262.9	54.1	1.5	13.8	11.1	0.7	32.8	502.6	13.5
	SD	183873.6	262.8	84.1	1871.4	1762.7	4853.3	56.5	4.9	27.0	32.4	1.6	81.9	1519.9	16.2
Py2	Min.	504.3	0.03	0.4	0.3	0.4	0.8	1.3	0.001	0.01	0.01	0.003	0.18	4.4	0.04
	Max.	628068.7	691.2	71.7	4175.3	10966.2	28718.4	95.7	7.8	58.4	107.2	10.8	128.9	925.3	164.7
n = 23	Mean	472151.9	241.6	19.8	502.3	496.5	2073.2	29.1	0.4	10.0	10.2	1.1	19.4	209.1	23.4
	SD	184396.1	181.8	17.9	1014.4	2282.6	6110.6	29.7	1.6	13.9	25.6	2.4	28.1	286.5	36.9

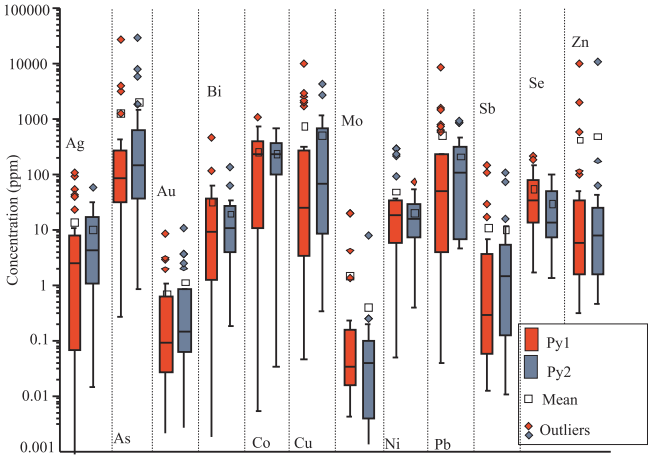

Fig. 11. Comparative box plot of the LA-ICP-MS data of two generations of pyrite, illustrating the concentration ranges of specific trace elements and highlighting subtle differences.

salient barbed patterns despite the flat iron signal in the LA-ICP-MS time-resolved depth profiles (Fig. 14), suggesting that the silver, bismuth, galena and gold compounds occur as nano-size inclusions. The Ag signals in the LA-ICPMS time-resolved depth profiles are comparable to those of Co, Pb, Bi and Cu (Fig. 14b), and show positive correlations with Au, Sb, and Pb (Fig. 13), indicating that the silver is closely related to the formation of nanoparticles of bismuth, stibnite (antimonite), tetrahedrite (or chalcopyrite), and galena, as is the case with the common occurrence of matildite and argyrythrose inclusions in galena (Cook et al., 1998; Tang et al., 2019). The close relationship between galena and silver has been recognized in numerous hydrothermal and magmatic ore deposits (Costagliola et al., 2003; Li et al., 2016).

Silver can be integrated into tetrahedrite by solid state exchange reactions to form argentiferous grains (Sack et al., 2003; Li et al., 2016). Like silver, Au signals show clear multi-spikey patterns in the LA-ICPMS time-resolved depth profiles (Fig. 14b), and there is a positive relationship between Ag and As (Figs. 14 and 13, respectively).

Py2 occurs as euhedral to subhedral or anhedral to subhedral grains without zoning, but Py2c shows slightly higher and variable concentrations of trace elements, such as Zn (0.4–110,000 ppm), As (0.8–28,700 ppm) and Au (0.003–10.8 ppm), but significantly low and variable concentrations of Co (0.03–691 ppm), Ni (0.4–712 ppm), Cu (0.3–4175 ppm), Ag (0.1–58 ppm), Bi (0.18–129 ppm), and Pb (4.4–925 ppm). Trace element profiles of Py2 show time resolved depth profiles similar to those of Py1 with slight differences in some trace element signals such as Pb, Ag, and Cu (Fig. 14d). The strong positive correlations between Ag and Sb, Ag and Cu (Fig. 13d, e) indicate that most silver occurs as inclusions in Sb compounds (argyrythrose, matildite) in galena or as solid solution in such minerals, as well as native Ag, which is consistent with the petrographic observations (Fig. 6f)

5.2. Origin of pyrite

Electron probe microanalyses and laser ablation-inductively coupled plasma mass spectrometry analyses reveal that different generations of sulfides have characteristic of major and trace element patterns (i.e., Co/Ni ratios), which can be used as a proxy for the distinct between origins of ore deposit. Carstens (1941) suggested that sedimentary pyrite has < 100 ppm Co and a C o: N i ratio < , whereas hydrothermal pyrite generally contains > 400 ppm Co and a Co: Ni ratio > 1. Pyrite of volcanic origin associated with Pb and Zn mineralization has low concentrations of Ni, very low concentrations of Co (< 10 ppm) and Co: Ni ratios < 1 (Loftus-Hills and Solomon, 1967). Price (1972) proposed that Co: Ni ratios in pyrite from massive sulphide deposits of volcanic origin are characterized by Co: Ni ratios between 5 and 50 (with an average of 8.7). Therefore, the trace element chemistry (e.g. Co/Ni ratios) and sulfur isotopic compositions of pyrite are widely used to distinguish the origin of pyrite and explain the genesis of hydrothermal ore deposits (Bajwah et al., 1987; Li et al., 2014; Reich et al., 2016). A Co/Ni ratio of less than 1 (average 0.63) is commonly taken to indicate syn-sedimentary pyrite (Barbour, 1961; Clark et al., 2004; Price, 1972), whereas Co/Ni ratios greater than one indicate that the pyrite is of hydrothermal origin. However, geological evidence must also be considered, such as mineralogical characteristics and the genetic type of ore deposit, when evaluating the origin of pyrite because some hydrothermal pyrites have Co/Ni ratios less than 1 (Bierlein et al., 2016). In this study the Co/Ni ratios of Py1 and Py2 are in the range of 0.02 – 57 (average 14), and 0.04 – 165 (average 23), respectively, indicating that the pyrite was precipitated from magmatic-hydrothermal fluids (Fig. 15). Nickel concentrations in pyrite can also provide information on the character of the pyrite-precipitating fluid. These are thought to mainly to reflect the primary fluid compositions, although these can be modified by wall rock/fluid interaction (Zhao et al., 2011). Ultramafic rocks contain high Ni concentrations 2200 ± 500 ppm (Palme & Jones, 2003), mafic rocks like MORB contain ~150 ppm Ni (Hofmann, 1988) whereas felsic rocks generally contain very low Ni concentrations (< 50 ppm; (Rudnick & Gao, 2003). In the Haweit gold deposit, the highest concentration of Ni in pyrite is 284 ppm in Py1, suggesting that the two types of pyrite were derived mainly from fluids that equilibrated with mafic and/or felsic material. The narrow range of $\delta^{34}S$ values of pyrite in the Haweit deposit (-3.3‰ to 3.4‰ for Py1 and −3.2‰ to 0.6‰ for Py2), indicate a magmatic sulfur source (Ohmoto, 1972; Rye & Ohmoto, 1974). The combination of trace element and isotopic data suggest that the pyrites were formed by hydrothermal fluids derived mainly from a mafic and/or felsic magmatic source.

5.3. Gold-arsenic distribution and relationships in pyrite in the Haweit gold deposit

In the Haweit deposit, pyrite is the main host mineral for gold. Gold occurs as nanoparticles of native gold and as solid solution with As in the pyrite. Based on the LA-ICPMS data, the two types of pyrite record slight differences in trace element contents and gold concentrations. The gold concentration in Py2 is slightly higher than that in Py1

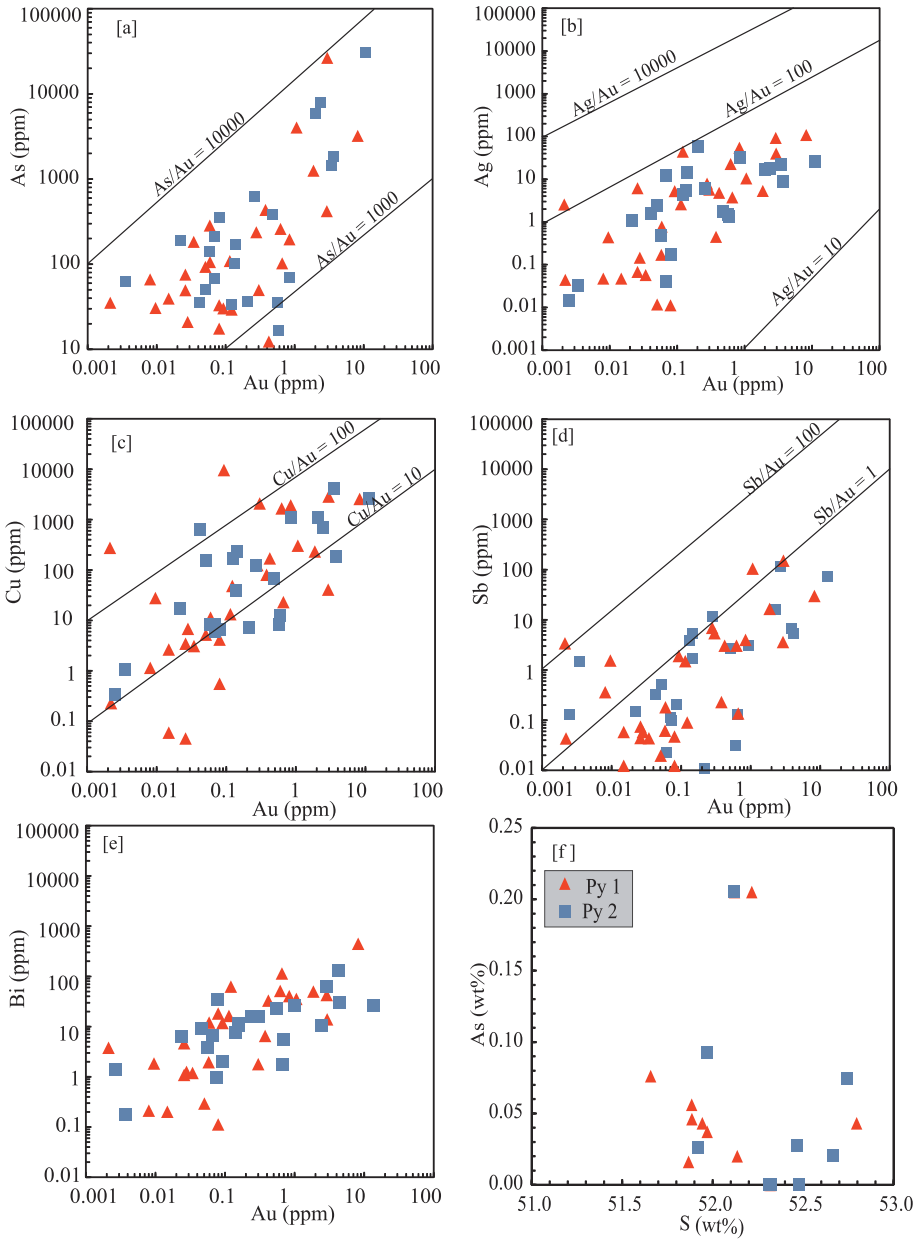

Fig. 12. Inter element correlations of selected trace elements in the two pyrite types of the Haweit gold deposit. (a) Au and As contents and Au/As ratios in pyrite. (b) Au and Ag contents and Au/Ag ratios in pyrite. (c) Au and Cu contents and Au/Cu ratios in pyrite. (d) Au and Sb contents and Au/Sb ratios in pyrite. (e) The correlation between Au and Bi contents in pyrite. (f) Figure showing no obvious correlation between S and As in pyrite.

(Table 3), indicating that gold mineralization was weaker during the early stage of mineralization (Py1). Generally, this gold occurs as invisible nanoparticles of separate Au-bearing phases (Large et al., 2007, 2009; Cook et al., 2009; Zhao et al., 2011). Py2 commonly contains both Au and Ag, with or without a relationship to As.

The correlation between Au and As dissolved in pyrite is well known in many gold deposits (Cook & Chryssoulis, 1990; Savage et al., 2000; Cline, 2001; Large et al., 2007, 2009). The Au-As relationship for the major pyrite types at the Haweit deposit (Fig. 12a) shows that most of the pyrite plots below the gold saturation line of Reich et al. (2005), suggesting that the gold is most likely in solid solution, as determined by the LA-ICPMS time-resolved depth profiles (Fig. 14).

5.4. Source of sulfur in the Haweit gold deposit

Sulfides in the Haweit deposit are predominately pyrite, chalcopyrite and arsenopyrite. The $\delta^{34}S$ value of ore-forming fluids and the sulfur isotopic compositions of sulfide minerals can be used to infer the degree of isotopic fractionation, the source of sulfur and the related physico-chemical conditions that prevailed in specific gold deposits (Ohmoto, 1972, 1986). Sulfur in gold-forming ore fluids may come from a variety of sources, including dissolved sulfur in seawater, pre-existing syngenetic/diagenetic sulfides in host rocks, or exsolved magmatic-hydrothermal solutions (Kerrich, 1986; Zoheir et al., 2019). These sulfur sources have overlapping values of $\delta^{34}S$ and so it is difficult to determine a specific source of sulfur for a gold deposit on the basis of sulfur isotopic analyses alone (Hodkiewicz et al., 2009).

Sulfur isotope ratios of pyrite from the Haweit deposit range from −3.3 to 3.4‰, with an average of −0.7%. This isotopic composition is mantle-like, and the slightly negative mean value is attributed to generation of isotopically light sulfur by rapid changes in oxidation state during ore fluid boiling due to the preferential oxidation of $H_2{}^{34}S$ (McKibben & Eldridge, 1990). This isotopic composition of sulfur could also be derived from a sulfur-bearing volatile magmatic phase that

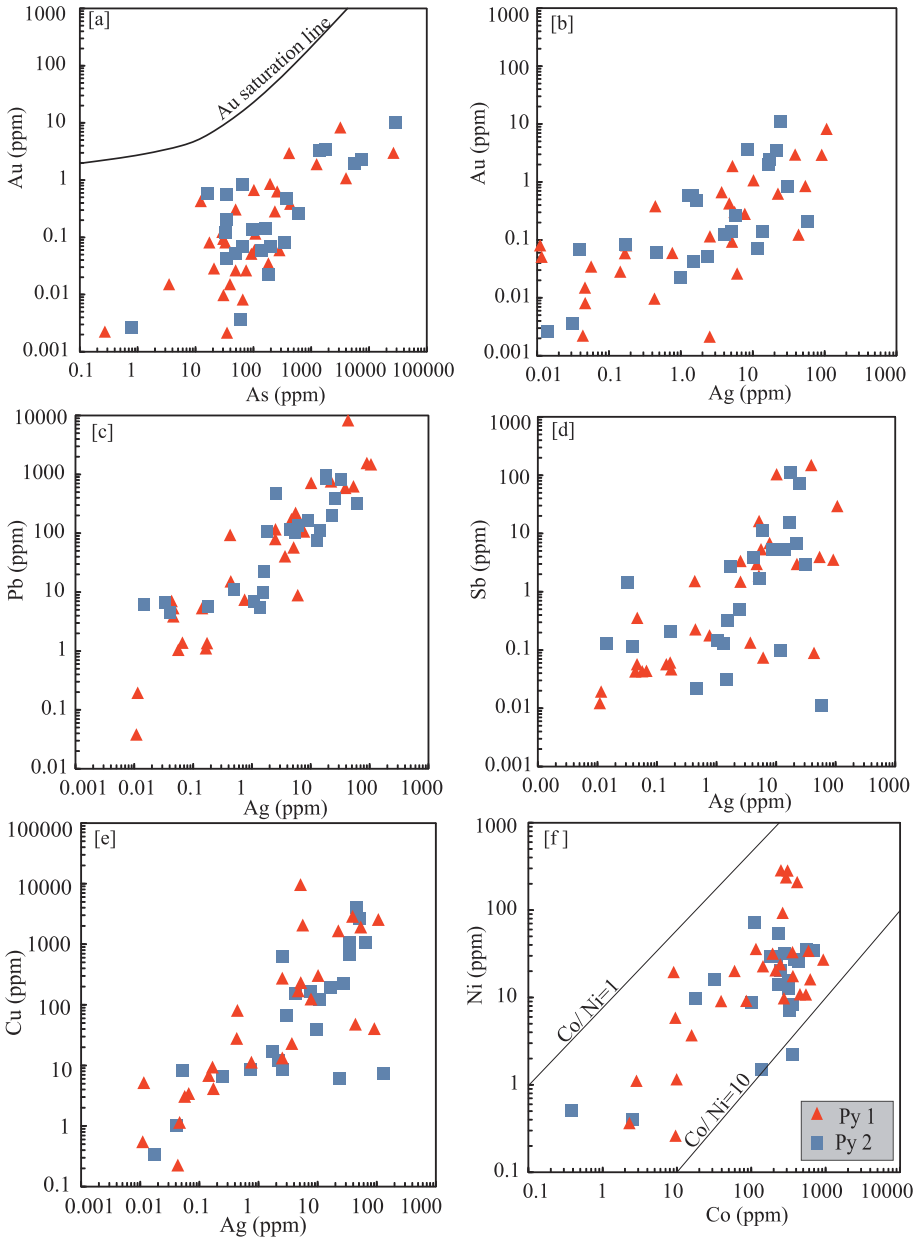

Fig. 13. Binary plots of selected trace elements in pyrite showing similarities between Py1 and Py2 (a) correlation between As and Au. (b) Positive correlation between Ag and Au. (c) Correlation between Ag and Pb (d) Positive correlation between Ag and Sb. (e) Positive correlation between Ag and Cu. (f) The Co and Cu contents and Co/Ni ratios.

unmixed upon cooling such that the reduced H_2S phase was enriched in ^{32}S and the oxidized H_2SO_4 phase was enriched in ^{34}S (Herzig et al., 1998), which is common in epithermal gold deposits (Arribas, 1995). A general coincidence in the sulfur isotope ratios of sulfides in both epithermal and porphyry environments reveals a common, magmatic component of the ore fluids in both of these mineralization systems. Furthermore, the coincidence in $\delta^{34}S$ values implies that any meteoric component to the epithermal ore fluids that mixed with magmatic fluids either scavenged very little sulfur from the host rock during infiltration or that the sulfur scavenged by meteoric fluids was isotopically similar to that hosted in porphyry-style mineralization.

Reduction of seawater sulfate can be a source of sulfur in ore-forming systems, however, that was not the case for Haweit mineralization. The $\delta^{34}S$ values of Py1 range from −3.3‰ to 3.4‰ with an average value of −0.3%, and $\delta^{34}S$ values of Py2 vary between −3.2‰ and 0.6‰ with an average value of −1.1% (Fig. 8). The similarities of the sulfur isotopic compositions between Py1 and Py2 suggest that the hydrothermal fluids were likely derived from the same reservoir. The sulfur isotopic data for the Haweit gold deposit also suggest derivation from a magmatic source, making this body similar to mesothermal gold deposits in many parts of the world (Kerrich, 1987; Trumbull et al., 2012; Gregory et al., 2014). The investigated pyrite samples yield that are in the range of the published sulfur isotopic data for most orogenic gold deposits worldwide (Groves et al., 1998; McCuaig and Kerrich, 1998; Kerrich et al., 2000; Goldfarb et al., 2001), and are also comparable to the orogenic gold deposits in the region, e.g., El Sid gold deposit −8.7% to 5.8%, Samut deposit 0.6 to 6.1% (Zoheir et al., 2019). The considerable evidence from geology and trace element composition of pyrite with sulfur isotopes allow us to suggest that the source of Haweit orogenic gold was magmatic-hydrothermal fluids.

6. Conclusions

Our textural observations on pyrite grains, coupled with the EPMA,

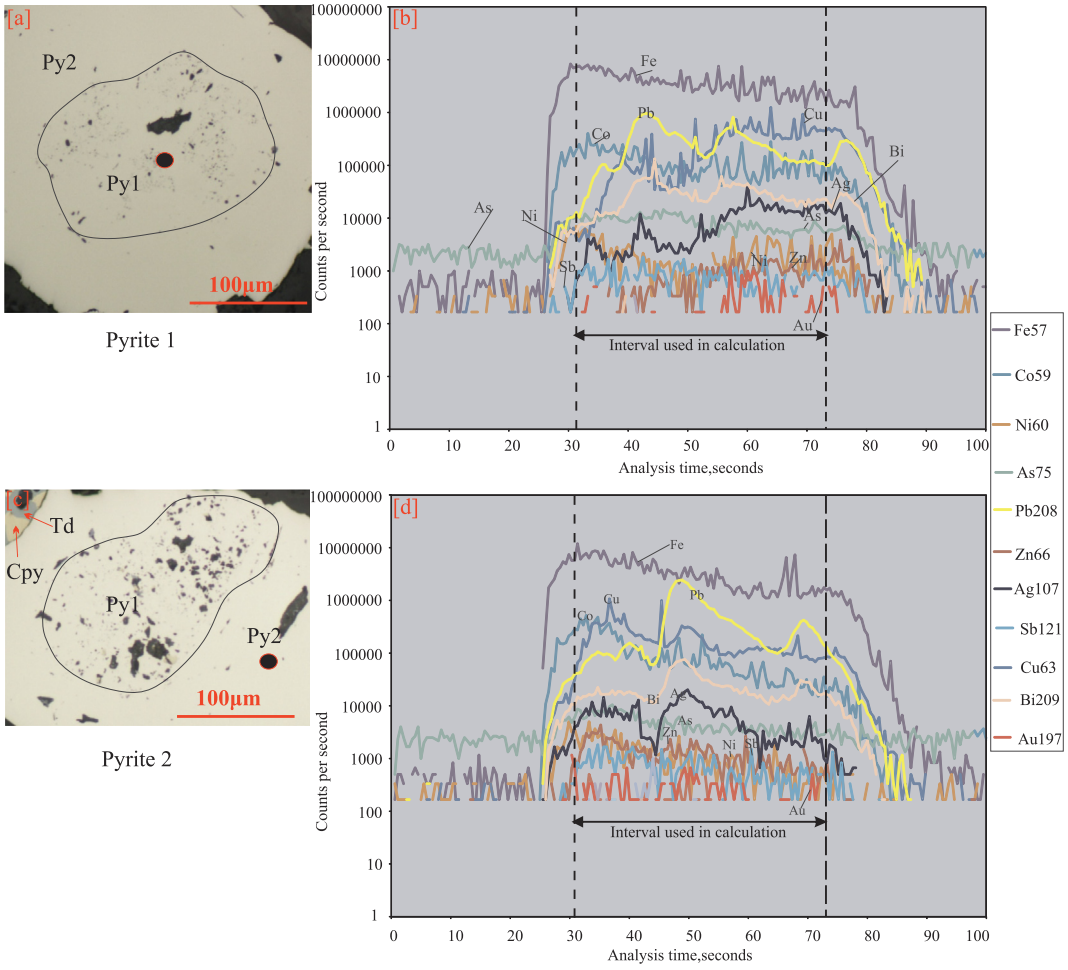

Fig. 14. Representative time-resolved depth profiles for pyrite analyzed in this study indicating the occurrences of gold and other major metal elements (a). Photomicrograph of Py1 with many inclusions enclosed in more homogeneous Py2. (b) A typical ICPMS multi-element counts output profile for data collected from Py1. (c) Photomicrograph of Py2 enclosing a core of Py1. (d) A typical ICPMS multi-element counts output profile for data collected from Py2.

LA-ICP-MS, and in-situ sulfur isotopic data, demonstrate the complexity of pyrites in the Haweit gold deposit, which reflect the evolution of hydrothermal events leading to formation of this orogenic gold deposit. These data allow us to reach the following conclusions:

1-. Hydrothermal pyrite grains in the Haweit deposit are classified into two types: fine-grained, anhedral, elongate to spongy grains (Py1), and medium- to coarse-grained, anhedral to subhedral grains (Py2).

2-. There are some trace element differences between the two pyrite types. Py1 contains slightly lower Au and As concentrations with

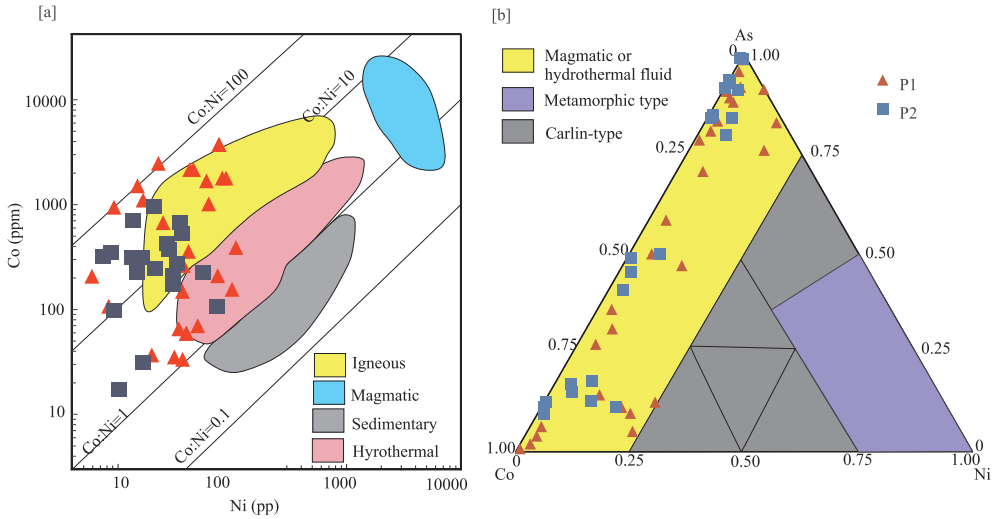

Fig. 15. Classification diagrams based on pyrite compositions, (a) The Ni-Co diagram of pyrite, showing comparison on the Haweit pyrite. (b) The As-Co-Ni diagram of pyrite in from Haweit gold deposit, pointing to a magmatic-hydrothermal origin. Modified after Baiwah et al,. (1987) and Brill (1989).

slightly higher Co, Ni and Cu, whereas Py2 grains record slightly higher and more variable concentrations of trace elements, such as Au, As, and Zn but have slightly lower and more variable concentrations of Co, Ni, Cu, Ag, Bi and Pb.

3-. A positive correlation between Au and As in the pyrite suggests that the gold is most probably held in solid solution.

4-. The narrow range of sulfur isotope compositions of the two pyrite types suggests that the hydrothermal fluids were homogeneous and were derived from the same magmatic sulfur source.

5-. Compatible elements (Ni and Co,) and sulfur isotopes of pyrite in the Haweit deposit suggest formation from hydrothermal fluids that originated from a mafic or felsic magmatic source.

Acknowledgments

This work was financially supported by the Research and Development Fund of China University of Geosciences, Wuhan (Grant No.:KH091908). We thank the Managers and the entire Geological Team of Alnawate Gold & Copper Mining Company (Haweit area) for their kind help with the fieldwork.

Appendix A. Supplementary data

Supplementary data to this article can be found online at https://doi.org/10.1016/j.oregeorev.2020.103405.

References

Abdelsalam, M.G., Liégeois, J.P., Stern, R.J., 2002. The Saharan metacraton. J. Afr. Earth Sci. 34 (3–4), 119–136.
Al-Hwaiti, M., Zoheir, B., Lehmann, B., Rabba, I., 2010. Epithermal gold mineralization at Wadi Abu Khushayba, southwestern Jordan. Ore Geol. Rev. 38 (1–2), 101–112.
Almond, D.C., Ahmed, F., Shaddad, M.Z., 1984. Setting of gold mineralization in the northern Red Sea Hills of Sudan. Econ. Geol. 79 (2), 389–392.
Arribas Jr, A., 1995. Characteristics of high-sulfidation epithermal deposits, and their relation to magmatic fluid. Mineral. Assoc. Canada Short Course 23, 419–454.
Bajwah, Z.U., Seccombe, P.K., Offler, R., 1987. Trace element distribution Co: Ni ratios and genesis of the Big Cadia iron-copper deposit, New South Wales, Australia. Mineral. Deposita 22 (4), 292–300.
Barbour, K.M., 1961. The Republic of the Sudan: a regional geography.
Barker, S.L., Cox, S.F., 2011. Oscillatory zoning and trace element incorporation in hydrothermal minerals: insights from calcite growth experiments. Geofluids 11 (1), 48–56.
Barker, S.L., Hickey, K.A., Cline, J.S., Dipple, G.M., Kilburn, M.R., Vaughan, J.R., Longo, A.A., 2009. Uncloaking invisible gold: use of nanoSIMS to evaluate gold, trace elements, and sulfur isotopes in pyrite from Carlin-type gold deposits. Econ. Geol. 104 (7), 897–904.
Belcher, R.W., Rozendaal, A., Przybylowicz, W.J., 2004. Trace element zoning in pyrite determined by PIXE elemental mapping: evidence for varying ore–fluid composition and electrochemical precipitation of gold at the Spitskop deposit, Saldania Belt, South Africa. X-Ray Spectrometry: Int. J. 33 (3), 174–180.
Bierlein, F.P., Reynolds, N., Arne, D., Bargmann, C., McKeag, S., Bullen, W., et al., 2016. Petrogenesis of a Neoproterozoic magmatic arc hosting porphyry Cu-Au mineralization at Jebel Ohier in the Gebeit Terrane, NE Sudan. Ore Geol. Rev. 79, 133–154.
Brill, B.A., 1989. Trace-element contents and partitioning of elements in ore minerals from the CSA Cu-Pb-Zn deposit, Australia, and implications for ore genesis. Can. Mineral. 27 (2), 263–274.
Carstens, C.W., 1941. Om geokjemiske undersøkelser av malmer. Norsk Geol. Tids 21, 213–221.
Ciobanu, C.L., Cook, N.J., Utsunomiya, S., Kogagwa, M., Green, L., Gilbert, S., Wade, B., 2012. Gold-telluride nanoparticles revealed in arsenic-free pyrite. Am. Mineral. 97 (8–9), 1515–1518.
Clark, C., Grguric, B., Mumm, A.S., 2004. Genetic implications of pyrite chemistry from the Palaeoproterozoic Olary Domain and overlying Neoproterozoic Adelaidean sequences, northeastern South Australia. Ore Geol. Rev. 25 (3–4), 237–257.
Cline, J.S., 2001. Timing of gold and arsenic sulfide mineral deposition at the Getchell Carlin-type gold deposit, north-central Nevada. Econ. Geol. 96 (1), 75–89.
Cook, N.J., Chryssoulis, S.L., 1990. Concentrations of invisible gold in the common sulfides. Can. Mineral. 28 (1), 1–16.
Cook, N.J., Spry, P.G., Vokes, F.M., 1998. Mineralogy and textural relationships among sulphosalts and related minerals in the Bleikvassli Zn-Pb-(Cu) deposit, Nordland, Norway. Mineral. Deposita 34 (1), 35–56.
Cook, N.J., Ciobanu, C.L., Mao, J., 2009. Textural control on gold distribution in As-free pyrite from the Dongping, Huangtuliang and Hougou gold deposits, North China Craton (Hebei Province, China). Chem. Geol. 264 (1–4), 101–121.
Costagliola, P., Di Benedetto, F., Benvenuti, M., Bernardini, G.P., Cipriani, C., Lattanzi, P.F., Romanelli, M., 2003. Chemical speciation of Ag in galena by EPR spectroscopy. Am. Mineral. 88 (8–9), 1345–1350.
Craig, J.R., Vokes, F.M., 1993. The metamorphism of pyrite and pyritic ores: an overview. Mineral. Mag. 57 (386), 3–18.
Craig, J.R., Vokes, F.M., Solberg, T.N., 1998. Pyrite: physical and chemical textures. Miner. Deposita 34 (1), 82–101.
Deditius, A.P., Utsunomiya, S., Renock, D., Ewing, R.C., Ramana, C.V., Becker, U., Kesler, S.E., 2008. A proposed new type of arsenian pyrite: composition, nanostructure and geological significance. Geochim. Cosmochim. Acta 72 (12), 2919–2933.
Deditius, A.P., Utsunomiya, S., Reich, M., Kesler, S.E., Ewing, R.C., Hough, R., Walshe, J., 2011. Trace metal nanoparticles in pyrite. Ore Geol. Rev. 42 (1), 32–46.
Deditius, A.P., Reich, M., Kesler, S.E., Utsunomiya, S., Chryssoulis, S.L., Walshe, J., Ewing, R.C., 2014. The coupled geochemistry of Au and As in pyrite from hydrothermal ore deposits. Geochim. Cosmochim. Acta 140, 644–670.
Dixon, T.H., Golombek, M.P., 1988. Late Precambrian crustal accretion rates in northeast Africa and Arabia. Geology 16 (11), 991–994.
Elsamani, Y., Almuslem, A.A., Tokhi, M.E., 2001. Geology and geotectonic classification of Pan-African gold mineralizations in the Red Sea Hills, Sudan. Int. Geol. Rev. 43 (12), 1117–1128.
Emsbo, P., Hofstra, A.H., Lauha, E.A., Griffin, G.L., Hutchinson, R.W., 2003. Origin of high-grade gold ore, source of ore fluid components, and genesis of the Meikle and neighboring Carlin-type deposits, northern Carlin trend, Nevada. Econ. Geol. 98 (6), 1069–1105.
Fleet, M.E., Mumin, A.H., 1997. Gold-bearing arsenian pyrite and marcasite and arsenopyrite from Carlin Trend gold deposits and laboratory synthesis. Am. Mineral. 82 (1–2), 182–193.
Fougerouse, D., Micklethwaite, S., Tomkins, A.G., Mei, Y., Kilburn, M., Guagliardo, P., et al., 2016. Gold remobilisation and formation of high grade ore shoots driven by dissolution-reprecipitation replacement and Ni substitution into auriferous arsenopyrite. Geochim. Cosmochim. Acta 178, 143–159.
Goldfarb, R.J., Groves, D.I., Gardoll, S., 2001. Orogenic gold and geologic time: a global synthesis. Ore Geol. Rev. 18 (1–2), 1–75.
Gregory, D., Meffre, S., Large, R., 2014. Comparison of metal enrichment in pyrite framboids from a metal-enriched and metal-poor estuary. Am. Mineral. 99 (4), 633–644.
Groves, D.I., Goldfarb, R.J., Gebre-Mariam, M., Hagemann, S.G., Robert, F., 1998. Orogenic gold deposits: a proposed classification in the context of their crustal distribution and relationship to other gold deposit types. Ore Geol. Rev. 13 (1–5), 7–27.
Hannington, M.D., 2014. Volcanogenic massive sulphide deposits. In: Holland, H.D., Turekian, K.K. (ed.) Treatise on geochemistry 2nd edition.
Hargrove, U.S., Stern, R.J., Kimura, J.I., Manton, W.I., Johnson, P.R., 2006. How juvenile is the Arabian-Nubian Shield? Evidence from Nd isotopes and pre-Neoproterozoic inherited zircon in the Bi'r Umq suture zone, Saudi Arabia. Earth Planet. Sci. Lett. 252 (3–4), 308–326.
Herzig, P.M., Hannington, M.D., Arribas Jr, A., 1998. Sulfur isotopic composition of hydrothermal precipitates from the Lau back-arc: implications for magmatic contributions to seafloor hydrothermal systems. Miner. Deposita 33 (3), 226–237.
Hodkiewicz, P.F., Groves, D.I., Davidson, G.J., Weinberg, R.F., Hagemann, S.G., 2009. Influence of structural setting on sulphur isotopes in Archean orogenic gold deposits, Eastern Goldfields Province, Yilgarn, Western Australia. Mineral. Deposita 44 (2), 129.
Hofmann, A., 1988. Chemical differentiation of the Earth: the relationship between mantle, continental crust, and oceanic crust. Earth Planet. Sci. Lett. 90, 297–314.
Hu, Z., Zhang, W., Liu, Y., Gao, S., Li, M., Zong, K., et al., 2014. "Wave" signal-smoothing and mercury-removing device for laser ablation quadrupole and multiple collector ICPMS analysis: application to lead isotope analysis. Anal. Chem. 87 (2), 1152–1157.
Johnson, P.R., Zoheir, B.A., Ghebreab, W., Stern, R.J., Barrie, C.T., Homer, R.D., 2017. Gold-bearing volcanogenic massive sulfide and orogenic-gold deposits in the nubian shield. S. Afr. J. Geol. 120, 63–76.
Keith, M., Häckel, F., Haase, K.M., Schwarz-Schampera, U., Klemd, R., 2016. Trace element systematics of pyrite from submarine hydrothermal vents. Ore Geol. Rev. 72, 728–745.
Kerrich, R., 1986. The stable isotope geochemistry of Au-Ag vein deposits in metamorphic rocks. In: Kyser, T.K. (Ed.), Mineralogical Association of Canada Short Course. Mineralogical Association of Canada, Saskatoon, pp. 287–1236.
Kerrich, R., 1987. The stable isotope geochemistry of Au-Ag vein deposits in metamorphic rocks. Mineral Assoc. Canada, Short Course Handbook 13, 287–336.
Kerrich, R., Goldfarb, R., Groves, D., Garwin, S., Jia, Y., 2000. The characteristics, origins, and geodynamic settings of supergiant gold metallogenic provinces. Sci. China, Ser. D Earth Sci. 43 (1), 1–68.
Kröner, A., Grieling, R., Reischmann, T., Hussein, I.M., Stern, R.J., Dürr, S., et al., 1987. Pan-African crustal evolution in the Nubian segment of northeast Africa. Proterozic Lithospheric Evol. 17, 235–257.
Kusky, T.M., Ramadan, T.M., 2002. Structural controls on Neoproterozoic mineralization in the South Eastern Desert, Egypt: an integrated field, Landsat TM, and SIR-C/X SAR approach. J. Afr. Earth Sci. 35 (1), 107–121.
Large, R.R., Maslennikov, V.V., Robert, F., Danyushevsky, L.V., Chang, Z., 2007. Multistage sedimentary and metamorphic origin of pyrite and gold in the giant Sukhoi Log deposit, Lena gold province, Russia. Econ. Geol. 102 (7), 1233–1267.
Large, R.R., Danyushevsky, L., Hollit, C., Maslennikov, V., Meffre, S., Gilbert, S., et al., 2009. Gold and trace element zonation in pyrite using a laser imaging technique: implications for the timing of gold in orogenic and Carlin-style sediment-hosted deposits. Econ. Geol. 104 (5), 635–668.
Li, N., Deng, J., Yang, L.Q., Goldfarb, R.J., Zhang, C., Marsh, E., et al., 2014. Paragenesis and geochemistry of ore minerals in the epizonal gold deposits of the Yangshan gold belt, West Qinling, China. Mineral. Deposita 49 (4), 427–449.
Li, Z.K., Li, J.W., Cooke, D.R., Danyushevsky, L., Zhang, L., O'Brien, H., et al., 2016.

Textures, trace elements, and Pb isotopes of sulfides from the Haopinggou vein deposit, southern North China Craton: implications for discrete Au and Ag–Pb–Zn mineralization. Contrib. Miner. Petrol. 171 (12), 99.
Liu, Y., Hu, Z., Gao, S., Günther, D., Xu, J., Gao, C., Chen, H., 2008. In situ analysis of major and trace elements of anhydrous minerals by LA-ICP-MS without applying an internal standard. Chem. Geol. 257 (1–2), 34–43.
Loftus-Hills, G., Solomon, M., 1967. Cobalt, nickel and selenium in sulphides as indicators of ore genesis. Miner. Deposita 2 (3), 228–242.
Maslennikov, V.V., Maslennikova, S.P., Large, R.R., Danyushevsky, L.V., 2009. Study of trace element zonation in vent chimneys from the Silurian Yaman-Kasy volcanic-hosted massive sulfide deposit (Southern Urals, Russia) using laser ablation-inductively coupled plasma mass spectrometry (LA-ICPMS). Econ. Geol. 104 (8), 1111–1141.
McClenaghan, S.H., Lentz, D.R., Cabri, L.J., 2004. Abundance and speciation of gold in massive sulfides of the Bathurst Mining Camp, New Brunswick, Canada. Can. Mineral. 42 (3), 851–871.
McCuaig, T.C., Kerrich, R., 1998. P—T—t—deformation—fluid characteristics of lode gold deposits: evidence from alteration systematics. Ore Geol. Rev. 12 (6), 381–453.
McKibben, M.A., Eldridge, C.S., 1990. Radical sulfur isotope zonation of pyrite accompanying boiling and epithermal gold deposition; a SHRIMP study of the Valles Caldera, New Mexico. Econ. Geol. 85 (8), 1917–1925.
Mikhlin, Y.L., Romanchenko, A.S., 2007. Gold deposition on pyrite and the common sulfide minerals: an STM/STS and SR-XPS study of surface reactions and Au nanoparticles. Geochim. Cosmochim. Acta 71 (24), 5985–6001.
Monecke, T., Petersen, S., Hannington, M. D., Grant, H., Samson, I., 2016. The minor element endowment of modern sea-floor massive sulfide deposits and comparison with deposits hosted in ancient volcanic successions. Society of Economic Geologists.
Morey, A.A., Tomkins, A.G., Bierlein, F.P., Weinberg, R.F., Davidson, G.J., 2008. Bimodal distribution of gold in pyrite and arsenopyrite: examples from the Archean Boorara and Bardoc shear systems, Yilgarn Craton, Western Australia. Econ. Geol. 103 (3), 599–614.
Mumin, A.H., Fleet, M.E., Chryssoulis, S.L., 1994. Gold mineralization in As-rich mesothermal gold ores of the Bogosu-Prestea mining district of the Ashanti Gold Belt, Ghana: remobilization of "invisible" gold. Miner. Deposita 29 (6), 445–460.
Muntean, J.L., Cline, J.S., Simon, A.C., Longo, A.A., 2011. Magmatic–hydrothermal origin of Nevada's Carlin-type gold deposits. Nat. Geosci. 4 (2), 122.
Ohmoto, H., 1972. Systematics of sulfur and carbon isotopes in hydrothermal ore deposits. Econ. Geol. 67 (5), 551–578.
Ohmoto, H., 1986. Stable isotope geochemistry of ore deposits: Rev., 491–556.
Palme, H., Jones, A., 2003. Solar system abundances of the elements. Treatise Geochem. 1.41-61, 1.41-61.
Peng, B., Frei, R., 2004. Nd-Sr-Pb isotopic constraints on metal and fluid sources in W-Sb-Au mineralization at Woxi and Liaojiaping (Western Hunan, China). Miner. Deposita 39 (3), 313–327.
Peterson, E.C., Mavrogenes, J.A., 2014. Linking high-grade gold mineralization to earthquake-induced fault-valve processes in the Porgera gold deposit, Papua New Guinea. Geology 42 (5), 383–386.
Price, B.J., 1972. Minor elements in pyrites from the smithers map area, bc and exploration applications of minor element studies Doctoral dissertation, University of British Columbia.
Rahman, E.M.A., 1993. Geochemical and geotectonic controls of the metallogenic evolution of selected ophiolite complexes from the Sudan. Reimer.
Reclus, J.J.É., 1876. The earth and its inhabitants. The universal geography. In: Ravenstein, E.G., Keane, A.H. Vol. 8. JS Virtue.
Reich, M., Becker, U., 2006. First-principles calculations of the thermodynamic mixing properties of arsenic incorporation into pyrite and marcasite. Chem. Geol. 225 (3–4), 278–290.
Reich, M., Kesler, S.E., Utsunomiya, S., Palenik, C.S., Chryssoulis, S.L., Ewing, R.C., 2005. Solubility of gold in arsenian pyrite. Geochim. Cosmochim. Acta 69 (11), 2781–2796.
Reich, M., Deditius, A., Chryssoulis, S., Li, J.W., Ma, C.Q., Parada, M.A., et al., 2013. Pyrite as a record of hydrothermal fluid evolution in a porphyry copper system: a SIMS/EMPA trace element study. Geochim. Cosmochim. Acta 104, 42–62.
Reich, M., Simon, A.C., Deditius, A., Barra, F., Chryssoulis, S., Lagas, G., et al., 2016. Trace element signature of pyrite from the Los Colorados iron oxide-apatite (IOA) deposit, Chile: a missing link between Andean IOA and iron oxide copper-gold systems? Econ. Geol. 111 (3), 743–761.
Rocci, G., 1965. Essai d'interpretation de mesures geochronologiques. La structure de l'Ouest africain. Sci. Terre 10 (3–4), 461–478.
Rudnick, R.L., Gao, S., 2003. Composition of the continental crust. Treatise Geochem. 3, 659.
Rye, R.O., Ohmoto, H., 1974. Sulfur and carbon isotopes and ore genesis: a review. Econ. Geol. 69 (6), 826–842.
Sack, R.O., Lynch, J.V.G., Foit, F., 2003. Fahlore as a petrogenetic indicator: Keno Hill Ag-Pb-Zn District, Yukon, Canada. Mineral. Mag. 67 (5), 1023–1038.
Sami, M., Ntaflos, T., Farahat, E.S., Mohamed, H.A., Ahmed, A.F., Hauzenberger, C., 2017. Mineralogical, geochemical and Sr-Nd isotopes characteristics of fluorite-bearing granites in the Northern Arabian-Nubian Shield, Egypt: constraints on petrogenesis and evolution of their associated rare metal mineralization. Ore Geol. Rev. 88, 1–22.
Savage, K.S., Tingle, T.N., O'Day, P.A., Waychunas, G.A., Bird, D.K., 2000. Arsenic speciation in pyrite and secondary weathering phases, Mother Lode gold district, Tuolumne County, California. Appl. Geochem. 15 (8), 1219–1244.
Schandelmeier, H., Darbyshire, D.P.F., Harms, U., Richter, A., 1988. The E Saharan craton: evidence for pre-Pan-African crust in NE Africa W of the Nile. The Pan-African belts of NE Africa and Adjacent areas. Friedr Vieweg and Sohn, 69–94.
Stern, R.J., 1994. Arc assembly and continental collision in the Neoproterozoic East African Orogen: implications for the consolidation of Gondwanaland. Annu. Rev. Earth Planet. Sci. 22 (1), 319–351.
Stern, R.J., Kröner, A., 1993. Geochronologic and isotopic constraints on Late Precambrian crustal evolution in NE Sudan. J. Geol. 101, 555–574.
Stern, R.J., Nielsen, K.C., Best, E., Sultan, M., Arvidson, R.E., Kröner, A., 1990. Orientation of late Precambrian sutures in the Arabian-Nubian shield. Geology 18 (11), 1103–1106.
Stoeser, D.B., Camp, V.E., 1985. Pan-African microplate accretion of the Arabian Shield. Geol. Soc. Am. Bull. 96 (7), 817–826.
Sung, Y.H., Brugger, J., Ciobanu, C.L., Pring, A., Skinner, W., Nugus, M., 2009. Invisible gold in arsenian pyrite and arsenopyrite from a multistage Archaean gold deposit: Sunrise Dam, Eastern Goldfields Province, Western Australia. Mineral. Deposita 44 (7), 765.
Sykora, S., Cooke, D.R., Meffre, S., Stephanov, A.S., Gardner, K., Scott, R., et al., 2018. Evolution of pyrite trace element compositions from porphyry-style and epithermal conditions at the Lihir gold deposit: implications for ore genesis and mineral processing. Econ. Geol. 113 (1), 193–208.
Tang, L., Hu, X.K., Santosh, M., Zhang, S.T., Spencer, C.J., Jeon, H., et al., 2019. Multistage processes linked to tectonic transition in the genesis of orogenic gold deposit: a case study from the Shanggong lode deposit, East Qinling, China. Ore Geol. Rev. 111, 102998.
Thomas, H.V., Large, R.R., Bull, S.W., Maslennikov, V., Berry, R.F., Fraser, R., et al., 2011. Pyrite and pyrrhotite textures and composition in sediments, laminated quartz veins, and reefs at Bendigo gold mine, Australia: insights for ore genesis. Econ. Geol. 106 (1), 1–31.
Tolessa, D., Pohl, W., 1999. Constraints on interpretation of geochemical data for gold exploration in multiply deformed and metamorphosed areas: an example from Legadembi gold deposit, southern Ethiopia. J. Afr. Earth Sc. 29 (2), 367–380.
Trumbull, R.B., Morteani, G., Li, Z., Bai, H., 2012. Gold metallogeny. The Sino-Korean Platform. Springer Science & Business Media.
Vail, J.R., 1988. In: Tectonics and Evolution of the Proterozoic basement of NE Africa. The Pan-African belts of NE Africa and Adjacent areas. Friedr Vieweg and Sohn, pp. 185–226.
Voute, F., Hagemann, S.G., Evans, N.J., Villanes, C., 2019. Sulfur isotopes, trace element, and textural analyses of pyrite, arsenopyrite and base metal sulfides associated with gold mineralization in the Pataz-Parcoy district, Peru: implication for paragenesis, fluid source, and gold deposition mechanisms. Miner. Deposita 1–24.
Ward, J., Mavrogenes, J., Murray, A., Holden, P., 2017. Trace element and sulfur isotopic evidence for redox changes during formation of the Wallaby Gold Deposit, Western Australia. Ore Geol. Rev. 82, 31–48.
Zhao, H.X., Frimmel, H.E., Jiang, S.Y., Dai, B.Z., 2011. LA-ICP-MS trace element analysis of pyrite from the Xiaoqinling gold district, China: implications for ore genesis. Ore Geol. Rev. 43 (1), 142–153.
Zhu, Z.Y., Jiang, S.Y., Ciobanu, C.L., Yang, T., Cook, N.J., 2017. Sulfur isotope fractionation in pyrite during laser ablation: implications for laser ablation multiple collector inductively coupled plasma mass spectrometry mapping. Chem. Geol. 450, 223–234.
Zoheir, B.A., Johnson, P.R., Goldfarb, R.J., Klemm, D.D., 2019. Orogenic gold in the Egyptian Eastern Desert: Widespread gold mineralization in the late stages of Neoproterozoic orogeny. Gondwana Res.
Zong, K., Klemd, R., Yuan, Y., He, Z., Guo, J., Shi, X., et al., 2017. The assembly of Rodinia: the correlation of early Neoproterozoic (ca. 900 Ma) high-grade metamorphism and continental arc formation in the southern Beishan Orogen, southern Central Asian Orogenic Belt (CAOB). Precambr. Res. 290, 32–48.